JGR Atmospheres

RESEARCH ARTICLE
10.1029/2019JD031313

Practical and Intrinsic Predictability of a Warm-Sector Torrential Rainfall Event in the South China Monsoon Region

Naigeng Wu[1,2,3], Xiaoran Zhuang[1], Jinzhong Min[1], and Zhiyong Meng[3]

[1]Key Laboratory of Meteorological Disaster of Ministry of Education, Nanjing University of Information Science and Technology, Nanjing, China, [2]Key Laboratory of Regional Numerical Weather Prediction, Institute of Tropical and Marine Meteorology, China Meteorological Administration, Guangzhou, China, [3]Laboratory for Climate and Ocean-Atmosphere Studies, Department of Atmospheric and Oceanic Sciences, School of Physics, Peking University, Beijing, China

Key Points:
- Both the practical and intrinsic predictability of a coastal warm sector torrential rainfall event during the Southern China Monsoon Rainfall Experiment (SCMREX) are investegated
- The occurrence of warm-sector rainfall is closely related to the nighttime strengthened (cooling) monsoon flow (temperature) over the sea (mountain)
- The warm-sector rainstorm could be near the point of bifurcation, where predictability is intrinsically limited

Correspondence to:
N. Wu and X. Zhuang,
wunaigeng@hotmail.com;
zxrxz3212009@163.com

Citation:
Wu, N., Zhuang, X., Min, J., & Meng, Z. (2020). Practical and intrinsic predictability of a warm-sector torrential rainfall event in the South China monsoon region. *Journal of Geophysical Research: Atmospheres*, *125*, e2019JD031313. https://doi.org/10.1029/2019JD031313

Received 7 JUL 2019
Accepted 23 DEC 2019
Accepted article online 3 JAN 2020

Abstract Warm-sector torrential rainfall (WR) in the South China monsoon region has long been a forecasting challenge because of the limited capability of numerical models in heavy rainfall without strong synoptic forcing. Through convection-allowing ensemble forecasts, this study explores both the intrinsic and practical predictability of a coastal WR event on 19–20 May 2015 during SCMREX (the Southern China Monsoon Rainfall Experiment). The results show a large variability in forecast performance among different members, indicating the practical limit of predictability. In general, GOOD members tend to have a stronger low-level southerly wind over the sea (monsoon flow) and a considerable surface cooling over the northern mountains (associated with land/mountain breeze). Further investigation via ensemble-based sensitivity analysis shows that the occurrence of WR is closely related to the nighttime strengthened (cooling) southerly wind (temperatures) over the sea (mountains), 1–3 hr prior to the convection initiation. In contrast, spatial scaling of the initial perturbations has little impact on the forecast after 3 hr and the meso-γ-scale rainfall is fully decorrelated after 12 hr, suggesting an intrinsic predictability limit for lead times as short as 6–12 hr. Sensitivity experiments are conducted with the initial-condition differences reduced by almost an order of magnitude smaller than typical ensemble perturbations, with the results demonstrating that the rainstorm might be near the point of bifurcation, where predictability is intrinsically limited. The limits of both intrinsic and practical predictability highlight the need for rapidly updated and probabilistic convection-allowing ensemble forecasts for events of this type.

1. Introduction

Throughout the world, extreme rainfall events and the often associated flash flooding continue to threaten many facets of everyday life, including the infrastructure of the built environment, individual livelihoods, and personal safety. The South China coast—a crucial region in which the East Asian monsoon rainband originates and begins its seasonal march (Luo et al., 2017; Tao & Chen, 1987)—is an area with one of the highest frequencies of heavy rainfall in the world. In this region, in addition to the heavy rainfall associated with synoptic-scale fronts, there are also frequent torrential rainfall events that occur within weak synoptic disturbances far from (or without) frontal systems (known as warm-sector torrential rainfall; Huang et al., 1986; Ding, 1994). The warm-sector heavy rains in South China monsoon region are different from the so-called warm sector rainfall in midlatitudes, which often appears within the warm sector of a frontal cyclone/extratropical cyclone (i.e., after the warm front) and still being closely associated with fronts (Boustead et al., 2013; Browning et al., 1974; Markowski & Richardson, 2010; Oliver &; Shaw, 1956). Such warm-sector torrential rainfall in South China has long been a problem for forecasters owing to the limited capability of numerical models in predicting heavy rainfall without strong synoptic forcing.

Since the first scientific experiment regarding heavy rainfall in South China in the early 1980s, warm-sector torrential rainfall has attracted the attention of meteorologists. The impact of low-level warm and humid flow (e.g., Huang et al., 1986; Wang, Luo, et al., 2014), land-sea effects (e.g., Chen et al., 2014; Wu et al., 2017), terrain effects (e.g., Wu & Luo, 2016; Xu et al., 2012), and convective environmental conditions of mesoscale convective systems (MCSs; e.g., Xia et al., 2006; Zhang et al., 2011) have been emphasized. In recent years, using smaller spacing mesoscale observation data, several observation-based analyses have examined the structure, initiation, maintenance, and properties of warm-sector torrential rainfall–associated MCSs (e.g., Wang, Luo, et al., 2014; Wu & Luo, 2016; Liu et al., 2018). Planetary boundary layer (PBL) weather systems such as low-level jets, near-surface winds, and precipitation-generated cold outflows have been demonstrated to play important roles in initiating and maintaining warm-sector rainfall (Chen et al., 2017; Du & Chen, 2019; Wang, Luo, et al., 2014; Wu et al., 2017). Our recent statistical analysis (Wu et al., 2020) further revealed the relationship between formation/evolution of warm-sector heavy rainfall and the diurnal variability of multiscale land-sea effects (synoptic-scale monsoon flow and local land-sea breeze) and local orographic effect (lifting/blocking and mountain-valley breeze). The morning peak of warm-sector heavy rainfall is associated with the intensified convergence between nocturnal low-level jets in southerly monsoon and land breezes (Wu et al., 2019). An ensemble-based analysis of European Centre for Medium-Range Weather Forecasts (ECMWF) global ensemble forecast data showed that warm-sector torrential rainfall usually has a large ensemble-mean-amount bias and a relatively large spread, suggesting a significant difference in the predictability for warm-sector and frontal torrential rainfall events (Du & Chen, 2018). Despite recent advances in understanding the formation of this flash-flood-producing warm-sector torrential rainfall, little is known about its predictability in this region. Atmospheric predictability is a basic scientific issue related to the practical application of weather forecasting. The study of atmospheric predictability began with Thompson (1957) and Lorenz (1963, 1969), and then aroused the attention of meteorologists. According to the intrinsic property of error, broadly speaking, predictability can be broken down into two parts: intrinsic predictability and practical predictability. Intrinsic predictability is defined as “the extent to which prediction is possible if an almost perfect procedure is used” (e.g., Lorenz, 1969). Practical predictability refers to “the extent to which we ourselves are able to predict by the best-known procedure, either currently or in the foreseeable future” (e.g., Lorenz, 1982, 1996; Melhauser & Zhang, 2012; Nielsen & Schumacher, 2016). Therefore, the practical predictability of the atmosphere is affected by, but not equivalent to, the intrinsic predictability of the atmosphere. Moreover, both intrinsic predictability and practical predictability of the atmosphere are dependent on the specific atmospheric flow patterns that are in place (e.g., Lorenz, 1996; Zhang et al., 2006), with expected loss of predictability during regime transition (Palmer, 1993).

Most processes that govern torrential rainfall, especially in the warm season, reside in the mesoscale and storm-scale motions of the atmosphere. The increases in computing power in the early 2000s have fortunately allowed the simulation of mesoscale phenomena with higher horizontal resolution, meaning considerable efforts have been devoted to understanding the predictability of severe weather at the mesoscales and even smaller scales. Many studies on error growth at the mesoscale have indicated that deep moist convection is a primary mechanism for small-scale error growth (e.g., Hohenegger & Schär, 2007a, 2007b; Melhauser & Zhang, 2012; Nielsen & Schumacher, 2016; Zhang et al., 2003, 2006, 2007; Zhang et al., 2016). Moreover, small initial errors saturate at the convective scale and then grow upscale to limit the predictability at the mesoscale, resulting in error growth rates for high-resolution models being much higher than for coarser-resolution models (Hohenegger & Schär, 2007a). The notion of upscale error growth creating a limit on atmospheric predictability has gained wide acceptance in the meteorology community.

On the contrary, some studies have indicated that the error growth from very small scales can be masked by downscale error growth from larger scales and does not have a substantial impact on the limit of predictability (e.g., Bei & Zhang, 2007; Durran et al., 2013; Durran & Gingrich, 2014; Durran & Weyn, 2016; Rotunno & Snyder, 2008). Therefore, relative to the large-scale errors, these “butterflies” (very small initial errors) are not of practical importance in atmospheric predictability (Durran & Gingrich, 2014; Durran & Weyn, 2016). However, owing to direct energizing at the mesoscale by processes such as deep moist convection, the relevance to the real atmosphere of predictability estimates based on models of homogeneous turbulence is unclear (Bierdel et al., 2017; Sun & Zhang, 2016; Zhang et al., 2003). In fact, it is difficult to identify the rapid downscaling process of large-scale small errors (Durran & Weyn, 2016) and completely separate the upscale growth of small errors at the convective scale from the internal growth of large-scale errors (Sun & Zhang, 2016) in the real atmosphere. Moreover, Nielsen and Schumacher (2016) showed that both upscaling and downscaling effects of error growth exist, but even in the same weather process, the relative effects of these two error growth modes in different regions even on the same day are not the same.

Besides the initial condition (IC) errors, the practical atmospheric predictability of convective weather is influenced by errors in numerical weather prediction (NWP) models (Bauer et al., 2015; Burlingame et al., 2017; Stensrud et al., 2000; Wu et al., 2013), synoptic-scale forcing (Melhauser & Zhang, 2012; Zhang et al., 2015), environmental conditions (Cintineo & Stensrud, 2013; Park, 1999; Wandishin et al., 2008, 2010), topography (Walser et al., 2004; Zhang et al., 2015), and so on. Therefore, both the intrinsic predictability and practical predictability of convective weather events are highly case-/flow-/scale-dependent (Done et al., 2012; Hohenegger et al., 2006; Johnson et al., 2014; Nielsen & Schumacher, 2016; Walser et al., 2004). Even cases with a similar intensity of moist convection might exhibit a different predictability depending on the relationship between the larger-scale flow and the moist convection (Hohenegger et al., 2006). In order to further understand and improve the predictability of convective weather, the Mesoscale Predictability Experiment (MPEX) was conducted within the U.S. intermountain region and high plains (Weisman et al., 2015). Results from this experiment have shown that the spatial variability in PBL structure, which reflects the variability in low-level moisture, temperature, and winds, is very important to the predictability of convection initiation (CI; Weisman et al., 2015; Burlingame et al., 2017; Trapp & Woznicki, 2017).

The aforementioned mesoscale predictability studies on heavy rain focused primarily on midlatitude weather systems with strong baroclinicity, or warm-season extreme rainfall events with strong synoptic-scale forcing (e.g., fronts and/or associated upper-level troughs). In the tropical monsoon region, heavy-rain-producing systems and associated MCSs in the warm season usually possess strong convective/conditional instability but weak baroclinicity. The predictability of heavy rainfall events in this region (with strong moist convection), especially the frequent flash-flood-producing warm-sector torrential rains, has not yet been well documented. In this study, based on a typical warm-sector torrential rainfall event during the Southern China Monsoon Rainfall Experiment (SCMREX; Luo et al., 2017), we attempt to use convection-allowing ensembles (grid spacing down to 1 km) to understand the characteristics of error growth and mesoscale predictability of heavy rains at the monsoon coast.

The remainder of the paper is organized as follows. Section 2 presents an overview of the synoptic environment and evolution of the heavy rainfall event. Section 3 describes the model configuration and experimental design. The practical predictability and intrinsic predictability of the event are discussed in sections 4 and 5, respectively, and section 6 provides a summary and discussion.

2. Overview of the Warm-Sector Torrential Rainfall Event

The torrential rainfall that occurred during 19 to 20 May 2015 was one of the strongest heavy rain events during the “intensive observing periods” of SCMREX and was also one of the most disastrous heavy rainfall events to hit mainland China that year (Luo et al., 2017). The maximum rainfall occurred in Shanwei, a coastal city located in the southeast region of Guangdong Province, with a peak of 542 mm/day. This torrential rainfall event was mostly generated during the 12-hr period of 2000 LST 19 May to 0800 LST 20 May (LST = UTC + 8 hr). There were two heavy rainfall areas over South China: a large rainband located in the northern part of Guangdong and Guangxi, along with a narrow heavy-rain region located in the southeast coastal region (Figures 1a and 1b). These two heavy rainfall areas did not merge during the 12-hr period, though the northern rainband moved southeast with the cold front (Figure 1b).

The synoptic conditions combined to produce ingredients known to be conductive to heavy srainfall. From 2000 LST 19 May to 0800 LST 20 May, there was a synoptic cold front (with wind direction convergence and a large temperature gradient) at the surface extended southward form the northern areas to the central areas of South China (Figures 1c and 1d) and the northern rainband (Figures 1a and 1b) was located near the frontal region and its north side. Correspondingly, a wind shear line located over South China at the low levels. A strong low-level jet (with maximum wind speed exceeding 12 m/s) was present over South China Sea, advecting moisture northward toward the frontal region (Figures 1e and 1f). An upper-level weak shortwave trough was moving southeastward and Guangdong located in front of this trough, controlled by the southwesterly wind (Figure 1g). These synoptic conditions were closely associated with the northern rainband (frontal heavy rainfall). In contrast, the stronger coastal heavy rainfall occurred within the southerlies and far from the front (Figure 1), located at the warm-sector with the surface temperature exceeded 25°C (Figure 1c) and in the windward slopes of the coastal mountains. From a synoptic-scale perspective, relative to the frontal rainband occurring in the significant wind-direction convergence zone (similar to head-on

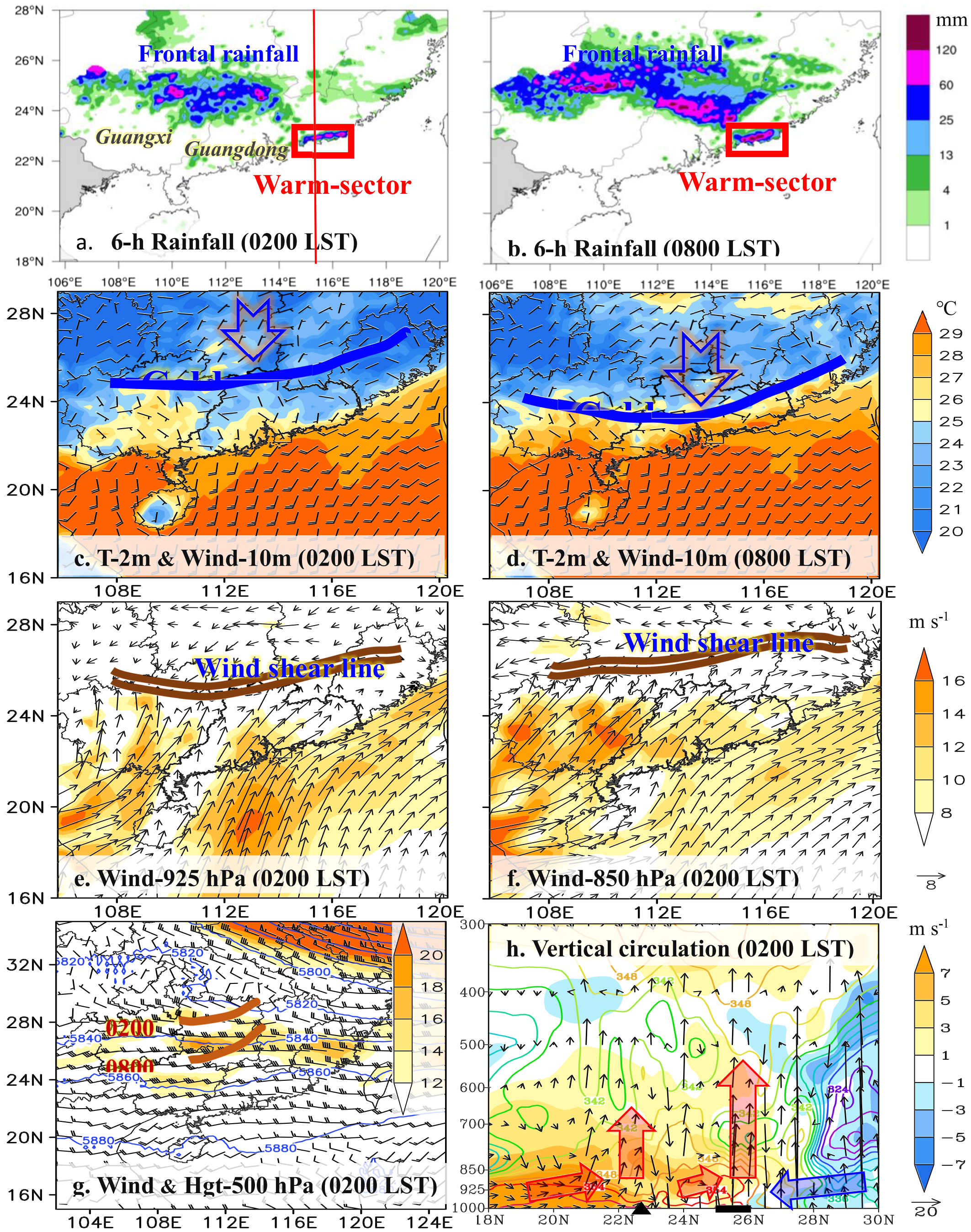

Figure 1. Distribution of (a and b) 6-hr cumulative precipitation based on rain gauge observations, (c and d) 2-m temperature and 10-m wind at 0200 LST and 0800 LST 20 May 2015, respectively, (e) 925-hPa wind, (f) 850-hPa wind, (g) 500-hPa wind and geopotential height, and (h) vertical circulation along 115.5°E at 0200 LST 20 May 2015. More specifically, panels (a) and (b) show the cumulative precipitation in the past 6 hr (shaded, mm), with the red rectangle identifying the location of the warm-sector torrential rainfall center; panels (c) and (d) show the center of the 2-m temperature (shaded, °C), with the blue solid lines marking the position of the cold front; panels (e) and (f) show the center of the 850-hPa wind speed (shaded, m/s), with the brown parallel lines marking the position of the wind shear line; panel (g) shows the center of the 500-hPa wind speed and geopotential height (contoured every 20 gpm), with the brown solid line making the position of westerly trough; and panel (h) show the merdional wind (shaded, m/s) and potential pseudo-equivalent temperatures (contoured every 3 K), with the solid triangles and squares making the latitudinal position of the warm-sector precipitation center and the front, respectively.

collision), the warm-sector heavy rainfall mainly occurs in the wind-speed convergence zone (similar to rear-end collision) of the boundary layer near 925 hPa (Figures 1e and 1h; Wu et al., 2017). The northern frontal rainband propagated southeastward with the front from Guangxi to Guangdong, beginning on the

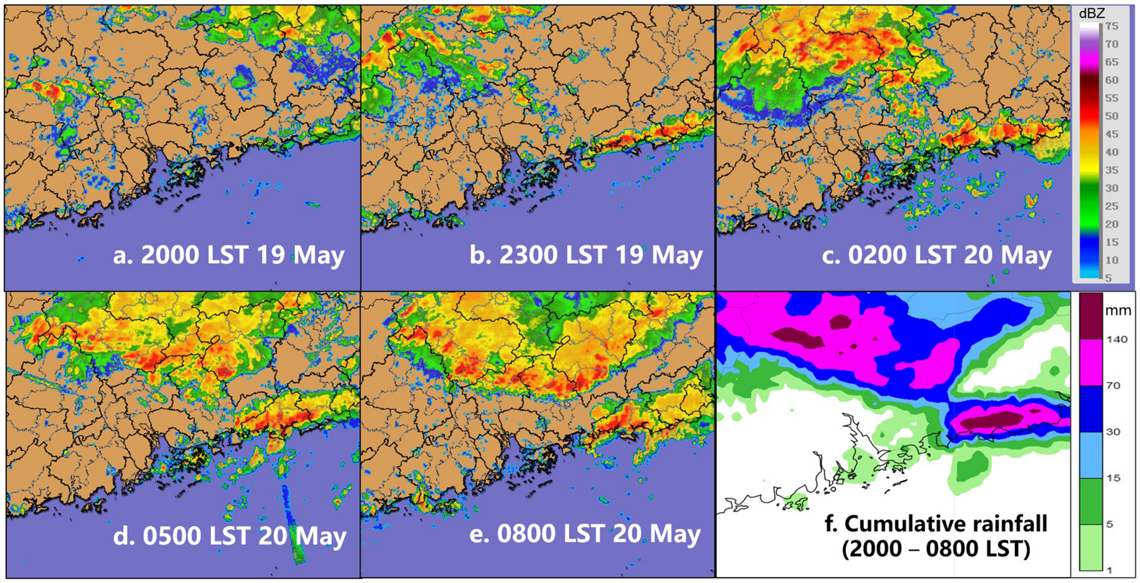

Figure 2. (a–e) Composite reflectivity (dBZ) of observations from 2000 LST 19 May to 0800 LST 20 May, and (f) cumulative rainfall (shaded, mm) of gauge–satellite merged precipitation analysis.

night (2300 LST) of 19 May, while the coastal heavy rains (warm-sector torrential rainfall) triggered in the southeast coastal areas during 2100–2300 LST and produced coherent rainfall for more than 12 h (Figure 2). From a smaller scale perspective with regional automatic weather stations, we can see more details that local land/mountain breeze (weak northerly wind) strengthened and intensified the convergence over the coastal areas might have some contribution to the warm-sector convection initiation/development (Figure 3; Wu et al., 2020).

Unlike the relatively good forecasting ability with respect to frontal rainbands, warm-sector heavy rainfall has long been a problem to forecasters owing to the limited capability of numerical models in predicting heavy rainfall without strong synoptic forcing. In operational forecasting, weather forecasters often do not know whether warm-sector torrential rain will occur, as well as when and where it will happen.

In this paper, based on previous studies and the case outlined above, we focus on the predictability of coastal warm-sector heavy rainfall, especially its convection initiation and development period before converging with the frontal rainbands (2000 LST 19 May to 0800 LST 20 May). We assume that the configuration and physics of the Weather Research and Forecasting (WRF) model can simulate such heavy rainfall process and therefore focus on the impact of initial-error growth on the practical and intrinsic predictability of warm-sector rainfall. Meanwhile, we attempt to use convection-allowing ensembles to understand the practical predictability of the key PBL weather systems to this coastal warm-sector heavy rainfall.

3. Methods and Experimental Design

3.1. Model Description

The numerical model utilized in this study was the fully compressible nonhydrostatic WRF model, version 3.8 (Skamarock & Coauthors 2008). Three two-way nested domains of 300 × 300, 499 × 499, and 532 × 502 horizontal grid points with 9-, 3-, and 1-km horizontal grid spacing, respectively, were employed. The largest domain (D01) covered the entire region of South China and the center-north of the South China Sea, while the innermost domain (D03) covered most of Guangdong Province (Figure 4a). There were 41 terrain-following hydrostatic-pressure vertical levels (including nine in the PBL bellow 850 hPa) and a model top of 10 hPa in all domains.

Several physical parameterization schemes were chosen for use in all three domains in all of the simulations, including the WSM6 microphysics scheme (Hong et al., 2004), the Yonsei State University PBL scheme (Hong et al., 2004), and a new version of the Rapid Radiative Transfer Model longwave and shortwave

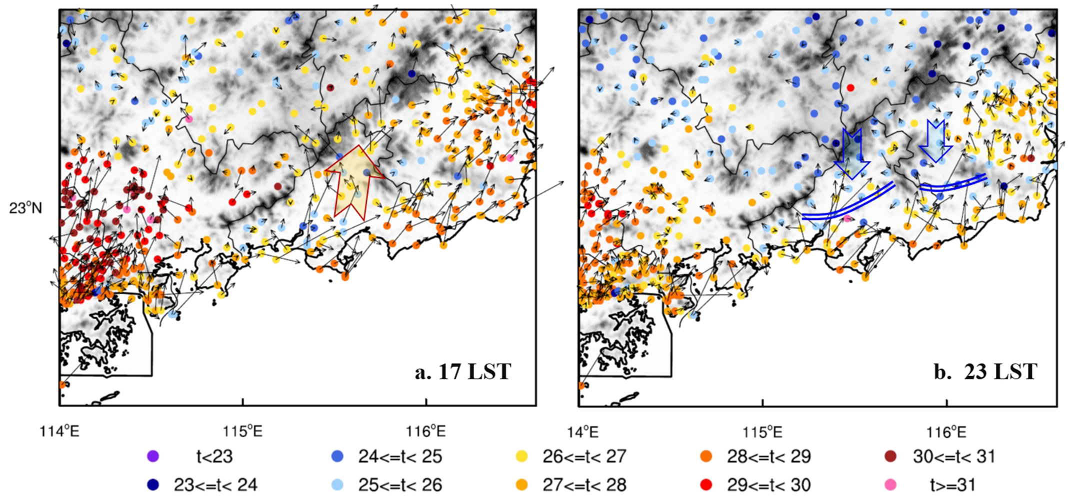

Figure 3. Distribution of 2-m temperature (solid dots) and 10-m wind at (a) 1700 LST and (b) 2300 LST 19 May 2015 based on regional automatic weather stations. Terrain heights are shaded in gray.

radiation scheme (Iacono et al., 2008). Additionally, the new Tiedtke cumulus parameterization scheme (Zhang & Wang, 2017) was used in the 9-km domain D01 and the 3-km domain D02.

The control deterministic forecast (CTRL) initialized the three model domains at 2000 LST 18 May and integrated until 2000 LST 20 May. The ICs and lateral boundary conditions (LBCs) of D01 were provided by National Centers for Environmental Prediction-Global Forecast System (NCEP-GFS) operational analysis data. The CTRL results showed that although the position and intensity of the rainband still have some errors compared with observation, the model successfully simulated both the frontal rainband and the warm-sector heavy rainfall (Figure 4c). It is indicated that this model setup has some capabilities of simulating this particular coastal warm-sector heavy rainfall and can refer to the "best-known procedure" to some extent. Therefore, in this paper, we focus on the IC uncertainties in the ensembles and investigate the feature of initial-error growth from both the practical and intrinsic perspective. The sensibility of the model physics and vertical/horizontal resolutions to the warm-sector heavy rainfall will be discussed in our future work.

3.2. Ensemble Generation

Two nested domains (D02 and D03) were employed in the ensemble generation. Considering the focus is on the impact of initial-error growth in the inner domain, one-way nesting was employed in all these ensemble experiments. For the outer 3-km resolution domain (D02), the initial ensemble is initialized at 0800 LST 19 May with a 24-hr forecast range by adding analysis perturbations (U, V, T, and Qv included; Toth & Kalnay,

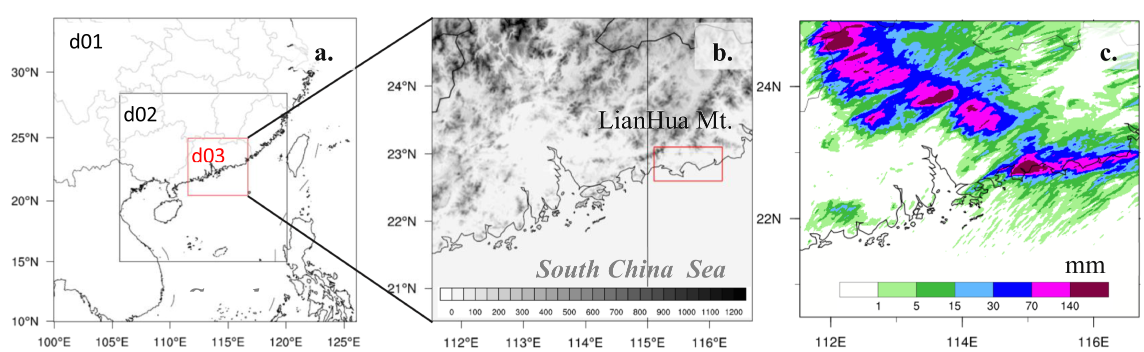

Figure 4. (a) Weather Research and Forecasting (WRF) domain configuration, with 9-, 3- and 1-km grid spacing for the d01, d02, and d03 domains, respectively. (b) Terrain height (shaded, m) in D03, wherein the red rectangle identifies the warm-sector torrential rainfall center. (c) Cumulative rainfall (shaded, mm) of the control deterministic forecast from 2000 LST 19 May to 0800 LST 20 May.

Table 1
Summary of the Initial Condition Perturbations (ICPs) Used in the Ensemble Experiments

Experiment	Members	ICPs
DOWN	20	Downscaling from the analysis perturbations from the ECMWF global ensemble prediction system (https://apps.ecmwf.int/datasets/)
ETR	20	Using the ETR method, the perturbations were incubated for 12 hr
BLEND	20	Blending of the DOWN scheme and ETR scheme (blending interval: 64–128 km)

Abbreviations: BLEND: blending method; DOWN: dynamical downscaling; ECMWF: European Centre for Medium-Range Weather Forecasts; ETR: Ensemble Transform with Rescaling.

1993; Wang, Bellus, et al., 2014) acquired from the first 20-member ECMWF global ensemble prediction products (https://apps.ecmwf.int/datasets/) through bilinear interpolation.

For the inner 1-km resolution domain (D03), three different methods for generating initial ensemble perturbations at different scales (Table 1) were employed to evaluate predictability in this study, and the ensemble experiments were initialized at 0800 LST 19 May with a 24-hr forecast range. These experiments employ the same LBC perturbations provided by the 24-hr outer domain ensemble forecasts. The first approach was dynamical downscaling (DOWN), which directly used the perturbations from the first 20-member ECMWF global ensemble prediction products as the 3-km ensembles. As depicted in Figure 5a, such perturbations had a horizontal resolution of 0.5°, showing good representation of synoptic-scale uncertainties (Hagedorn et al., 2012).

The second method was Ensemble Transform with Rescaling (ETR; Ma et al., 2014). The analysis perturbation X_a was updated from the forecast perturbation X_f via a transformation matrix $\mathbf{T}$:

$$X_a = X_f \mathbf{T}. \tag{1}$$

Detailed information about the calculation of $\mathbf{T}$ can be found in Wei et al. (2008). At each analysis state, the corresponding downscaled analysis perturbations from ECMWF global ensemble products were used to rescale the analysis perturbation after (1) via the rescaling factor γ,

$$\gamma = \begin{cases} \dfrac{\text{mask}}{\text{pertb}}, & \text{if mask} < \text{pertb} \\ 1, & \text{if mask} \geq \mathit{pertb} \end{cases}, \tag{2}$$

where "pertb" is the square-root of the total energy norm from X_a and "mask" denotes the root-mean-square of the total energy norm from downscaled perturbation. Note that such a method is able to maximize the effective degrees of perturbation freedom and constrain the amplitude of ICPs to vary in accordance with regional variations of analysis uncertainties with little computational cost. In this study, after adding downscaled perturbation to the analysis state at 2000 LST 18 May, a 3-hr interval ETR cycle was implemented, and the final updated perturbation at 0800 LST 19 May was used to initialize the ensemble experiments in ETR. Such ICPs encompassed flow-dependent convective-scale information (Figure 5b), which is believed to be essential in convective-scale ensemble prediction (Johnson & Wang, 2016).

The third approach was the blending method (BLEND), which was proposed by Wang, Bellus, et al. (2014) and involves combining larger-scale perturbations from LBCs with small-scale perturbations from ICPs via spatial filtering. Thus, to some extent, the blended ICPs should encompass multiscale uncertainties. In this work, the BLEND experiment was achieved by blending smaller-scale uncertainties from ETR and larger-scale uncertainties from DOWN via the discrete cosine transform method (Caron, 2013; Denis et al., 2002):

$$\text{IC}_{\text{blend}} = \text{IC}^{H}_{\text{ETR}} + \text{IC}^{L}_{\text{DOWN}}, \tag{3}$$

where the superscript H and L represent high- and low-pass filters, respectively. The blending interval was chosen as 64–128 km, indicating that the convective-scale uncertainties from ETR below 64 km and larger-

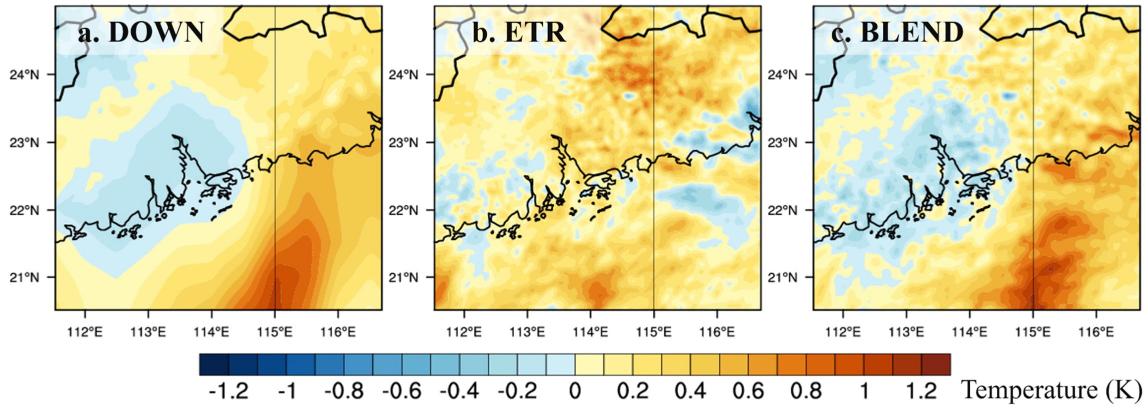

Figure 5. The initial temperature perturbations (at 850 hPa, shaded, K) of a corresponding member in the (a) dynamical downscaling (DOWN), (b) Ensemble Transform with Rescaling (ETR), and (c) blending method (BLEND) scheme.

scale uncertainties from DOWN above 128 km were totally retained in BLEND. Thus, BLEND encompassed both flow-dependent convective-scale uncertainties as well as reasonable larger-scale uncertainties (Figure 5c).

4. Practical Predictability: Uncertainties in the Simulated Torrential Rainstorm of the Convection-Allowing Ensembles

The practical predictability of the warm-sector torrential rainstorm based on the uncertainties of the 60-member convection-allowing ensemble (described in section 3a) will be examined in this section. The accurate prediction of CI is a problem that is highly sensitive to the interactions between the surface and free atmosphere that occur within the PBL (Stensrud, 2007). Previous mesoscale studies have also shown that low-level jet, land-sea breeze, mountain-valley wind, and terrain effects within the PBL play important roles in the occurrence of warm-sector heavy rainfall (Wang, Luo, et al., 2014; Wu & Luo, 2016; Wu et al., 2017). Thus, the practical predictability analysis of warm-sector torrential rainfall in this section focuses mainly on the uncertainties in the PBL.

4.1. Comparison of Rainstorm Forecasts Between "GOOD" and "POOR" Members

The 60-member ensemble initialized with the DOWN, ETR, and BLEND perturbations provided a wide variety of forecasts. Figure 6 shows the 3-hr accumulated rainfall from 2200 LST 19 May to 0100 LST 20 May of 30 ensemble members. This time was chosen because it shows the best subjectively chosen representation of the postconvective initiation. The images of different members show great CI differences in terms of the location of the warm-sector torrential rainfall center (red rectangle, as in Figure 1). Some members (e.g., BLEND02) did well in predicting the occurrence of warm-sector torrential rains, though some differences with observations regarding the intensity and location also existed. The model also produced members (e.g., ETR04) that did not trigger warm-sector convections (CI missed). The considerable differences among the members are shown more clearly in the temporal evolution of precipitation over the warm-sector torrential rainfall center (Figure 7). Relatively speaking, except for the first 3 hr, the DOWN and BLEND subsets exhibit greater dispersion (Figure 7) due to the synoptic-scale uncertainties of the ICs (Figure 5). The small spread (Table 2) of the ICs and striking variability of warm-sector torrential rains is a strong indicator of a chaotic divergence (and associated large forecast error growth) of these convection-allowing ensemble forecasts.

Focusing on the CI of the warm-sector rainfall, a subjective analysis of the ensemble members compared with observations was performed with determination of the spatial phasing and temporal phasing of the warm-sector convection. Five GOOD members (DOWN10, ETR12, ETR19, BLEND02, and BLEND10) and four POOR members (DOWN04, DOWN11, ETR04, and BLEND11) were selected as representations of forecast success and forecast failure for further detailed analysis (Figure 8). Figure 9 displays the PBL environments of the GOOD and POOR member averages at 2300 LST 19 May. The four rows of panels show the

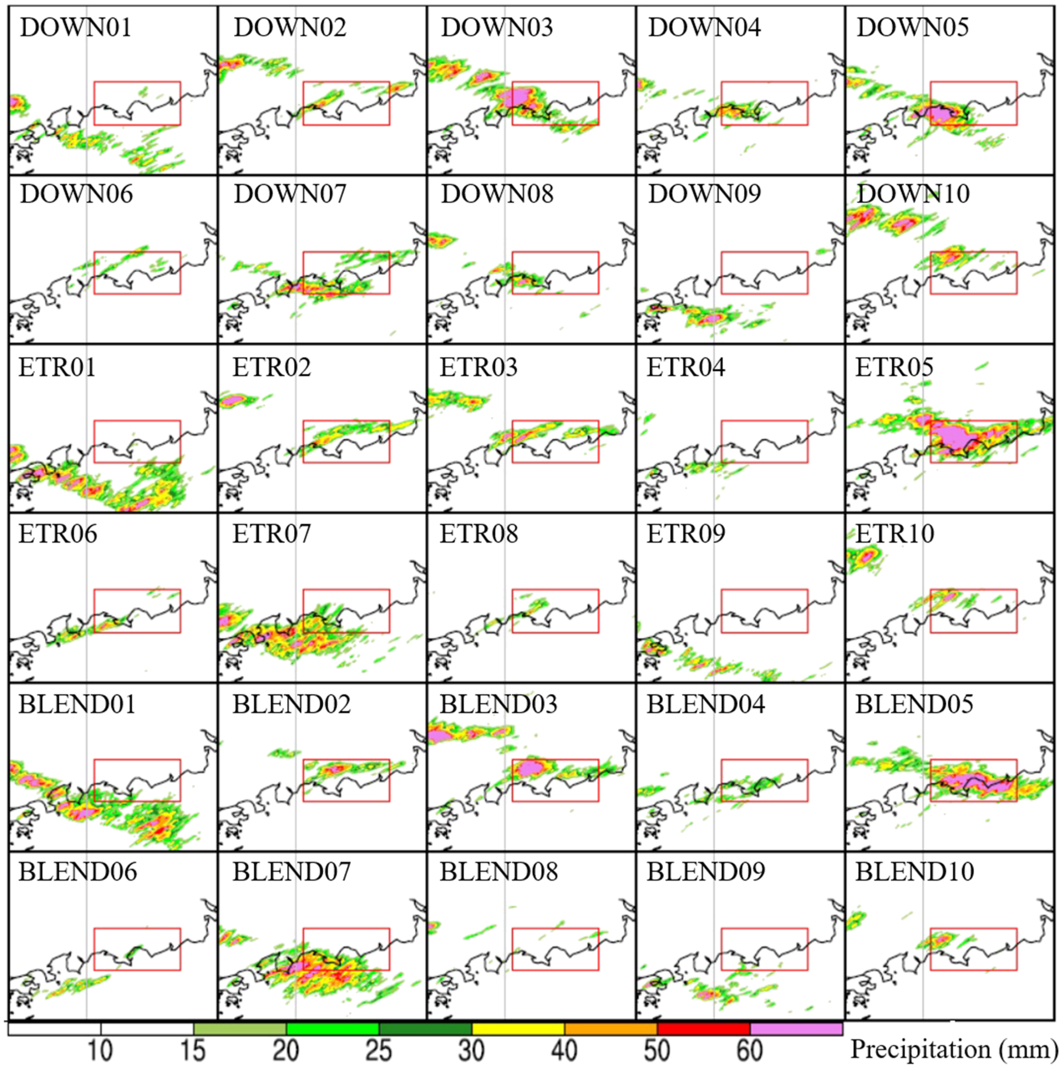

Figure 6. The simulated 3-h accumulated rainfall (shaded, mm) form 2200 LST 19 May to 0100 LST 20 May (postconvective initiation) of 30 members. The red rectangle in each panel identifies the location of the warm-sector torrential rainfall center (as in Figure 4).

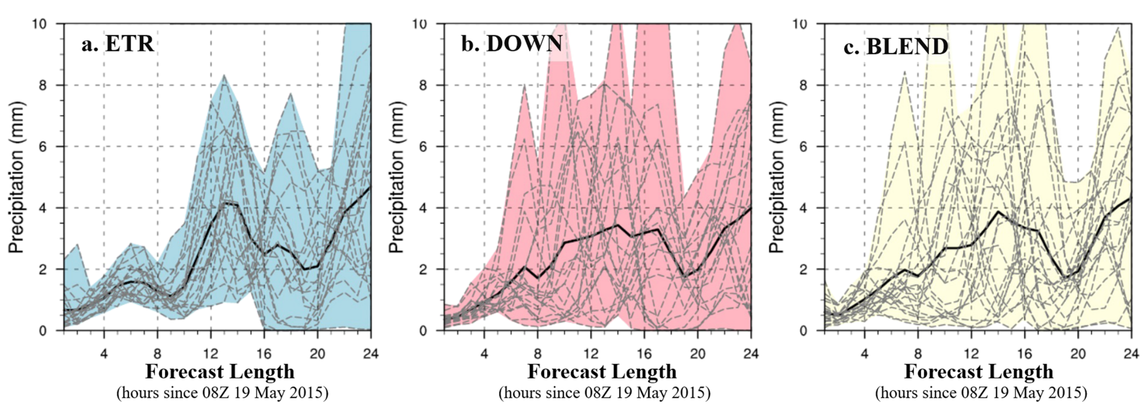

Figure 7. Temporal evolution of precipitation over the warm-sector torrential rainfall center in three subset ensemble forecast experiments. The grey dotted lines represent the forecasts of different members and the black solid lines the ensemble mean. The ensemble experiments were initialized at 0800 LST 19 May with a 24-hr forecast range.

Table 2
Domain-Average Standard Deviations of T, QV, U, and V in Different Experiments

Experiment	T (K)	QV (kg/kg)	U (m/s)	V (m/s)
DOWN	0.31	0.00030	0.77	0.74
ETR	0.35	0.00038	0.94	0.91
BLEND	0.20	0.00032	0.86	0.83

Abbreviations: BLEND: blending method; DOWN: dynamical downscaling; ETR: Ensemble Transform with Rescaling.

simulated 3-hr precipitation, 2-m temperature, 10-m wind, and 925-hPa wind, respectively. The red rectangles identify the observed warm-sector torrential rainfall center.

Although there were very small differences (e.g., T<0.5 K; wind-925 hPa <0.5 m/s) of the ICs between GOOD and POOR members (Table 2 and Figure 12), the CI over the next few hours varied widely. The location and timing of the CI of the coastal warm-sector rainfall can be captured by the GOOD member average (Figure a1), although the intensity of the heavy rains is slightly weaker than that of the rain-gauge observations. The POOR member average totally misses the coastal warm-sector heavy rainfall center in the south of the LianHua Mountains (LHM; Figure 9b1). The second (third) row in Figure 9 indicates that the near-surface temperatures (wind) over the surrounding areas of the LHM (north of the red rectangle) are cooler (weaker) in the GOOD members versus the POOR members. In contrast to the POOR members, there are 1–3°C (temperature) and 1–4 m/s (wind) negative differences over these mountain areas in the GOOD members. The 925-hPa wind for the averages of the GOOD members shows a stronger (1–4 m/s positive difference of wind speed) low-level jet over the northern South China Sea than that of the POOR members, resulted in more moisture and more unstable energy over the warm-sector heavy rainfall region in GOOD members. These simulated features are similar to results reported in previous studies based on case observations (Wang, Luo, et al., 2014; Wu & Luo, 2016) and statistics (Wu et al., 2017).

To further illustrate the effects of the PBL environment, the local vertical circulation and equivalent potential temperature (θ_{se}) in the center of the coastal warm-sector rainfall are shown (Figure 10). In contrast to the POOR members, it is apparent that the stronger low level southerly in the GOOD members brings abundant warm and moist air ($\theta_{se} > 362$ K) from the sea to the coastal areas, where the maximum difference of θ_{se} exceeds 6 K. Meanwhile, the θ_{se} near the surface over the mountains has a negative maximum difference of 3 K, resulting in a marked northerly mountain (land) breeze on the north side of the coastal line (Figure 10c). The southerly airflow over the sea and the mountain breeze over the land (Figures 10c, a3, and c3) result in apparent convergence and upward motion near the coastal line, which plays an important role in triggering

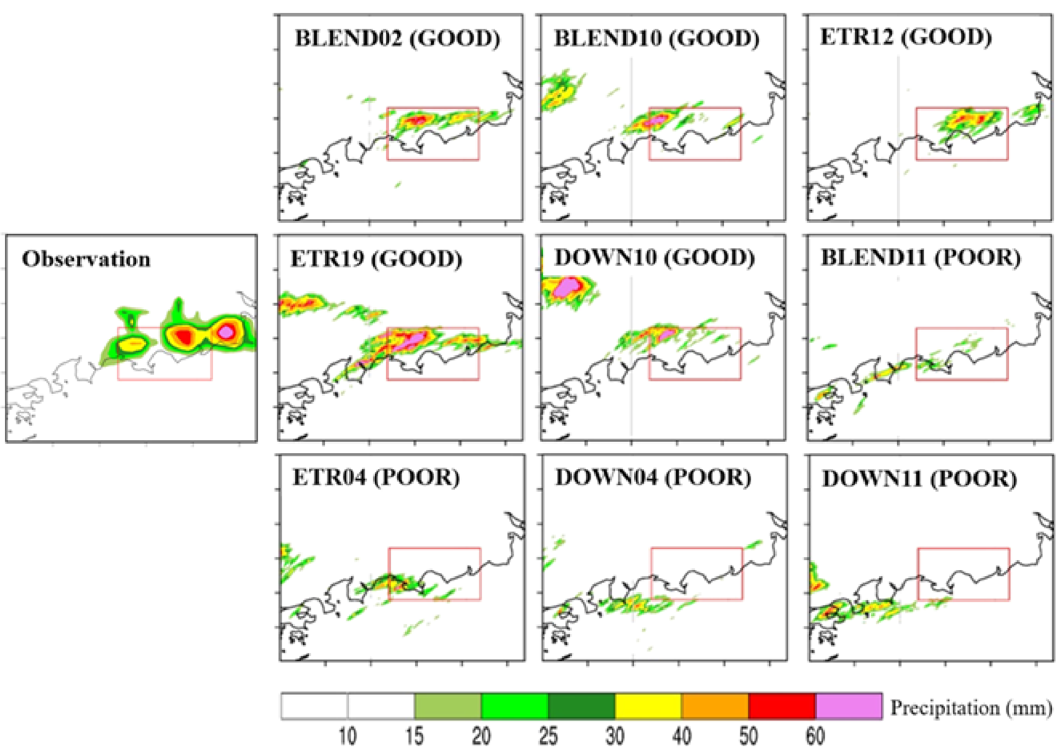

Figure 8. As in Figure 6 but for the (a–e) GOOD and (f–i) POOR members.

10.1029/2019JD031313

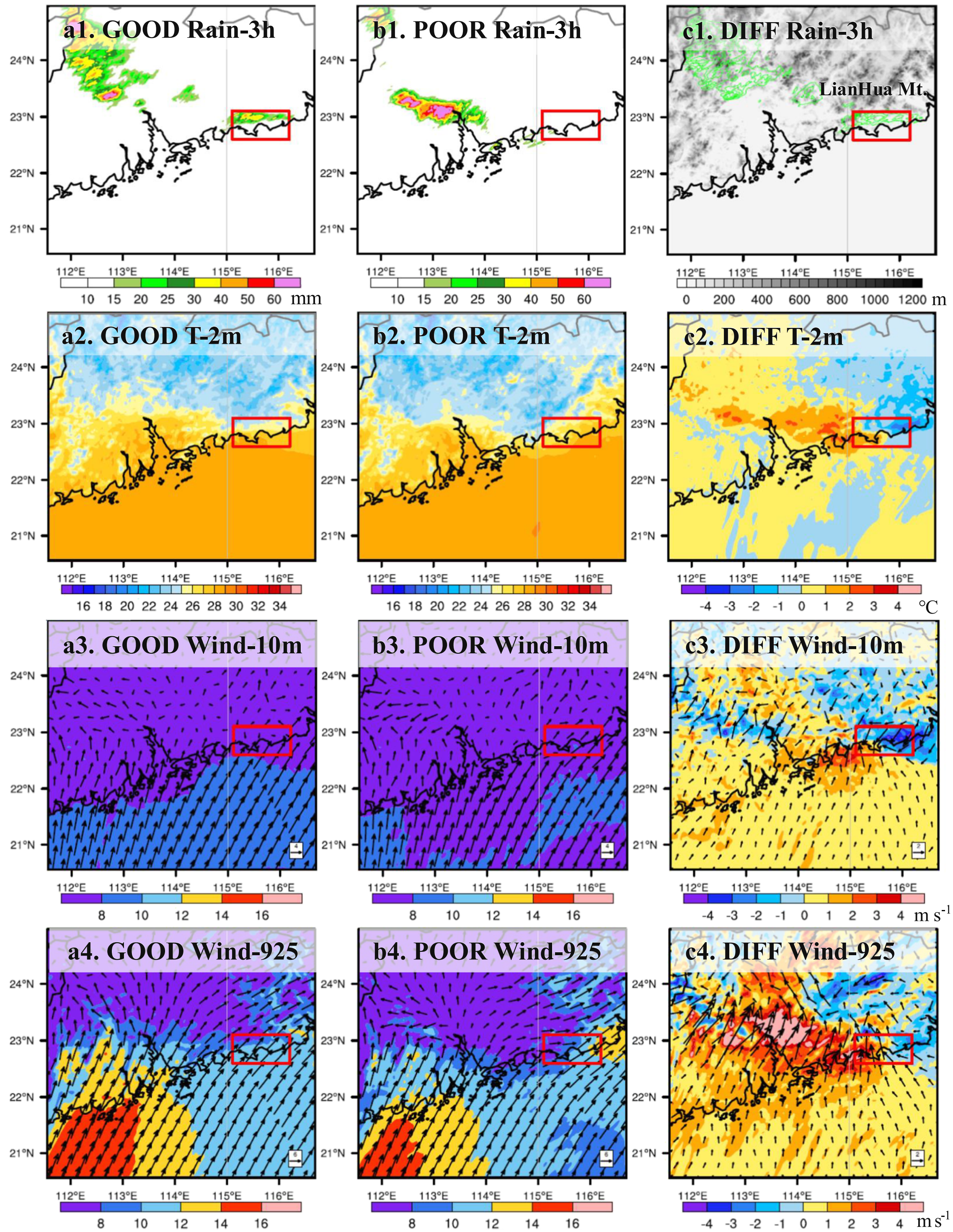

Figure 9. Environments of the GOOD and POOR member averages at 2300 LST 19 May (forecast hour 15, postconvective initiation) and their difference (DIFF, GOOD minus POOR): (a1, b1, and c1) the next 3 hr of precipitation (shaded in a1 and b1, green contours in c1, mm); (a2, b2, and c2) 2-m temperature (shaded, °C); (a3, b3, and c3) 10-m wind vectors and wind speed (shaded, m/s); (a4, b4, and c4) 925-hPa wind vectors and wind speed (shaded, m/s). The red rectangles identify the warm-sector torrential rainfall center (as in Figure 3).

the warm-sector torrential rainfall. These results suggest that the practical predictability of the coastal warm-sector rainfall is closely associated with the near-surface temperature/wind over the mountain areas and the low-level jets over the northern South China Sea.

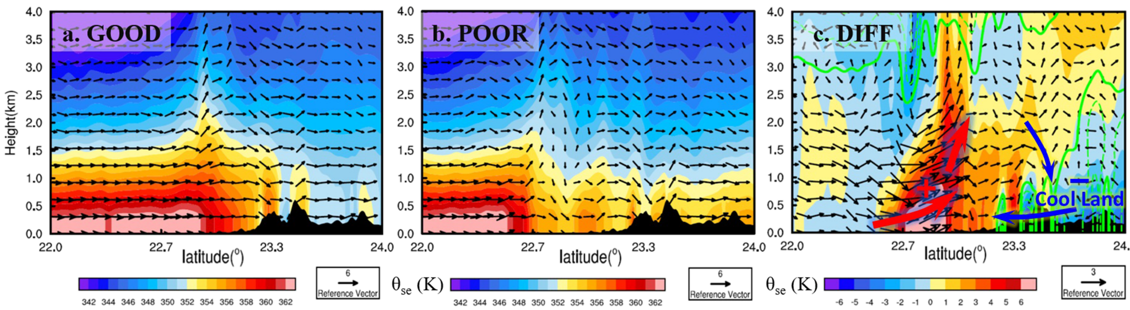

Figure 10. As in Figure 9 but for the local vertical circulation (vectors, m/s) and equivalent potential temperature (shaded, K) along 115.6°E (the warm-sector torrential rainfall center). The green lines represent the northerly wind (meridional wind <0 m/s, contoured every 0.5 m/s).

4.2. Ensemble Sensitivity Analysis of the Convection Initiation

In the previous section, the sensitivity of forecasts to ICPs by varying IC inputs for ensemble members were evaluated. Ensemble-based sensitivity analysis (ESA; Ancell & Hakim 2007; Torn & Hakim, 2008; Hakim & Torn, 2008) is a new and efficient tool for gaining quantitative insights and estimating the forecast sensitivity to the thermodynamic ICs or earlier forecast times. More recently, the use of ESA has been investigated for convection-permitting forecasting in the southern Great Plains region (Bednarczyk & Ancell, 2015; Hill et al., 2016), in MPEX (Torn & Romine, 2015; Weisman et al., 2015), and in China (Yu & Meng, 2016; Zhang & Meng, 2018). In the present study, ESA was applied to illustrate the forecast sensitivities of the CI of coastal warm-sector torrential rainfall to the thermodynamic conditions at earlier forecast times. By combining the ESA results with those of the ensemble variability analysis in section 4a, we attempt to shed more light on the practical predictability of the warm-sector torrential rainfall.

Figure 11 displays the ESA results for the warm-sector torrential rainfall center (response region, red rectangle) based on the 60-member convection-allowing ensemble. It shows that the precipitation within the response region is sensitive to the low-level thermodynamic characteristics southwest of the response region (green rectangle) and northern mountain areas (blue rectangle), beginning 3 and 2 hr prior to CI, respectively. The forecast is positively sensitive to 925-hPa (Figure 11, left-hand column) and near-surface (Figure 11, middle column) meridional wind, indicating that a strengthening of the southerly flow over the sea would produce a higher maximum simulated precipitation in the red rectangle region at hour 15 (2300 LST 19 May). Similarly, the significant negative sensitivity to near-surface temperature over the mountain areas (Figure 11, right-hand column) illustrates that a decrease in temperature over this region will produce more precipitation in the warm-sector torrential rainfall center 1–2 hr later. In contrast to the cooling of the mountainous areas, the impact of the strengthening of the low-level southerly wind over the sea on the CI of the warm-sector torrential rainfall has a longer lead time.

To further investigate the impacts of the low-level thermodynamic characteristics, the temporal evolutions of 925-hPa wind speed over the sea (green rectangle in Figure 11) and near-surface temperature over the mountains (blue rectangle in Figure 11) are shown (Figure 12). The temporal evolution of 925-hPa wind speed shows that the difference between GOOD and POOR members begins to be apparent after 2000 LST 19 May (Figure 12a). Compared to POOR members, the GOOD members exhibit a rapid increase in wind speed after 2000 LST 19 May, indicating that the nighttime strengthened southerly wind (monsoon flow) could be better captured by GOOD members. Similarly, the near-surface temperature over the mountain areas for GOOD and POOR members does not differ much in the first 8 hr (Figure 12b). After that time, the temperature for GOOD members shows a characteristic of rapid decline, while the temperature for POOR members exhibits a characteristic of decline that is approximately linear and slow. The maximum temperature difference between the two subsets reaches 2°C around 2000 LST 19 May. As shown in the observations of Figure 3, the thermal cooling from afternoon to night were much more pronounced in the mountain areas than in the coastal plains. This nighttime cooling temperature over the mountains increased temperature gradient near the coast, resulting in stronger near-surface land/mountain breezes over north side of the coastline and contributing to the convection initiation (combined with the strengthened low-level oceanic southerly flow). The subset-differences combined with this observe results showed that the nighttime cooling (related to the land/mountain breezes) could be better captured by the GOOD members.

10.1029/2019JD031313

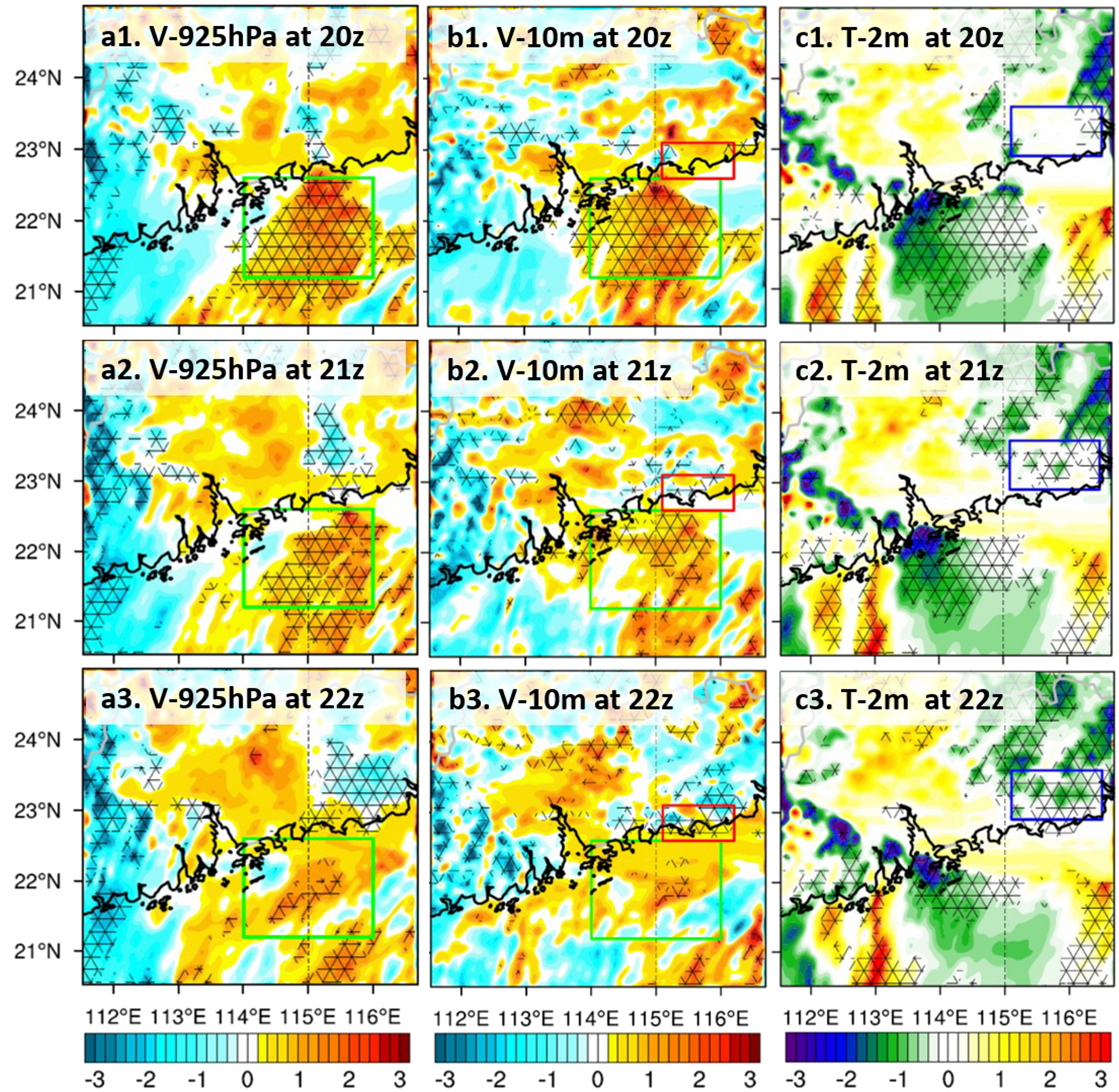

Figure 11. Sensitivity of hourly precipitation at 2300 LST 19 May (postconvective initiation) to (a1, a2, and a3) 925-hPa meridional wind [shaded, mm/(m/s)], (b1, b2, and b3) 10-m meridional wind [shaded, mm/(m/s)], and (c1, c2, and c3) 2-m temperature (shaded, mm/°C) at 2000, 2100, and 2200 LST. The red rectangle in each panel identifies the warm-sector torrential rainfall center. The blue and green rectangles highlight the sensitive regions discussed in the text. The black shading indicates regions where the sensitivity is statistically apparent at the 95% confidence level.

Moreover, the reason why rapid decline in temperature over mountain areas may be associated with the thermal diurnal cycle in mountain areas and the cold pool effect caused by the daytime precipitation, for which it should be further studied in the future.

Therefore, the ESA (section 4.2) and the subset-differences comparison (section 4.1) have confirmed similar conclusions in different aspects. Improvements of the associated physical processes for the nighttime strengthened southerly wind over the sea and nighttime cooling temperature over mountain areas are important to the practical predictability of warm-sector torrential rainfall.

5. Intrinsic Predictability: Sensitivity to Initial-Error Scale and Amplitude

In section 4, we demonstrated the sources of mesoscale practical predictability with a focus on the CI of coastal warm-sector torrential rainfall. Further model development, more observations, and advances in data assimilation will likely lead to better performing NWPs. However, it can also be seen that because of

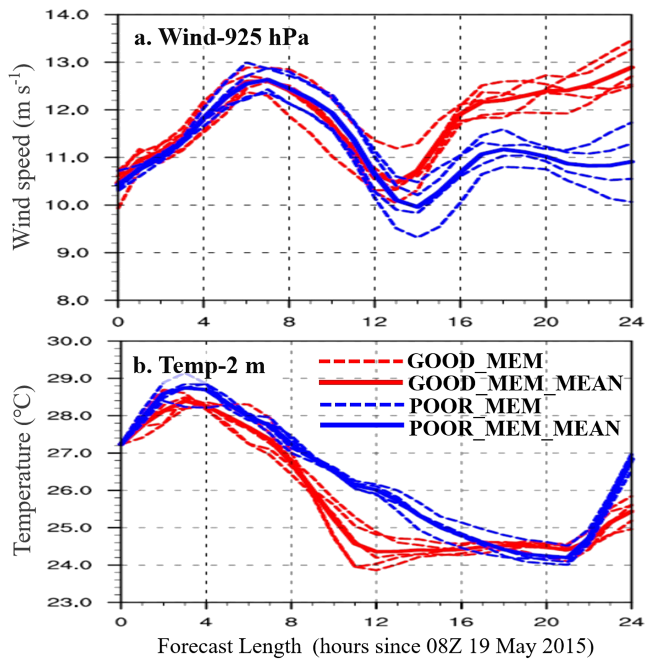

Figure 12. Temporal evolution of (a) 925-hPa wind speed (m/s, averaged within green rectangle region in Figure 8) and (b) 2-m temperature (°C, averaged within blue rectangle region in Figure 9) from 0800 LST 19 May to 0800 LST 20 May 2015. The red/blue dotted lines represent the GOOD/POOR members and the red/blue solid lines represent the mean of the GOOD/POOR members.

the chaotic nature of the atmosphere, very small initial errors in NWPs can grow rapidly and substantially contaminate the mesoscale forecast (Figure 12). In this section, we attempt to investigate the intrinsic predictability of this warm-sector torrential rainfall event.

5.1. Sensitivity to Initial-Error Scale and Error Growth at Different Scales

In this section, a quantitative method (Surcel et al., 2014, 2015) was employed to evaluate the error growth associated with spatial precipitation uncertainties and the sensitivity to initial-error scale. As mentioned in Surcel et al. (2015), by applying this methodology to two or more precipitation fields, a decorrelation scale λ_0 can be defined such that all scales smaller than λ_0 are fully decorrelated. For the scale $\lambda \leq \lambda_0$, there is no predictability of the model state (precipitation forecasts from ensemble members) for these scales. For the scale $\lambda \geq \lambda_0$, the ensemble forecast members are correlated, indicating some predictability by the ensemble. The power ratio of the decorrelation scale was defined in Surcel et al. (2015) as

$$R(\lambda) = \frac{\sum_{i=1}^{N} \mathrm{VAR}_{P_i}(\lambda)}{\mathrm{VAR}_{P_T}(\lambda)}, \tag{4}$$

where $\mathrm{VAR}_{P_i}(\lambda)$ is the variance of the precipitation field P_i at scale λ, $P_T = \sum_{i=1}^{N} P_i$ and N indicates the numbers of ensemble forecast members. The values for $R(\lambda)$ vary between 1, which represents complete decorrelation between the fields P_i at scale λ, and $1/N$, which represents perfect resemblance between the fields at scale λ. The value of λ_0 was determined by finding the largest λ for which $R(\lambda) \geq 0.90$. The threshold of 0.90 was chosen rather than 1 in this study as it was found to eliminate some of the noise in determining the decorrelation scale, without introducing any significant bias.

Figure 13 shows the power ratio of decorrelation scale at different forecast lead times in the DOWN, ETR, and BLEND experiments. The three color bands along the x axis mark the meso-γ scales (2–20 km), meso-β scales (20–200 km), and meso-α scales (200–2,000 km), respectively (Orlanski, 1975). The red reference lines indicate the threshold of 0.90, and the precipitation smaller than the corresponding scale will lost all the

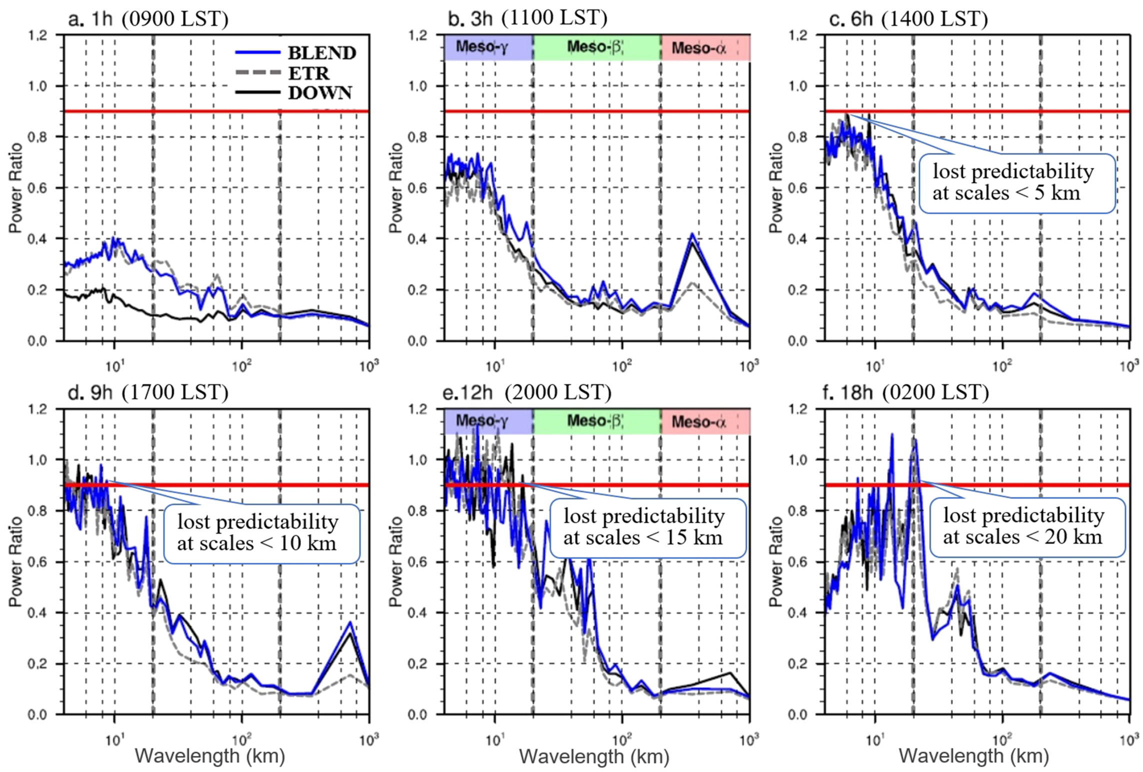

Figure 13. Power ratio of decorrelation scale at different forecast lead times (initialized at 0800 LST 19 May 2015) [(a) 1 hr, (b) 3 hr, (c) 6 hr, (d) 9 hr, (e) 12 hr, and (f) 18 hr] in the dynamical downscaling (DOWN; black line), Ensemble Transform with Rescaling (ETR; grey dashed line) and blending method (BLEND; blue line) experiments. The color bands along the *x* axis in (b) and (e) mark the different scales. The red reference lines indicate the threshold (total loss of predictability) of 0.90.

predictability when the power ratio exceeds this threshold. At the very beginning (Figure 13a), the power ratio of DOWN is much smaller than that of BLEND and ETR (at the scales smaller than $10^{1.7} \approx 50$ km). This may be related to the initial perturbations of DOWN members being from the global ECMWF model (50-km resolution), while ETR and BLEND members contain smaller storm-scale perturbations. Subsequently, the power ratio of all three experiments increases rapidly at the meso-γ scales (2–20 km; Figure 13b), which can be thought of as the small initial errors growing rapidly at small scales (Zhang et al., 2006; Zhang et al., 2016). After the first 3 hr, the power ratios increase rapidly and reach the threshold at different meso-γ scales (10 km at 6–9 hr and 20 km at 12–18 hr), indicating that the forecasts are fully decorrelated (lost predictability) at those scales (Figures 13c–13f). Furthermore, a considerable increase exists in the range of scales over which $R(\lambda) \geq 0.90$ with forecast lead time (about 5 km at 6 hr, 10 km at 9 hr, 15 km at 12 hr, and 20 km at 18 hr). Meanwhile, the power ratios of DOWN, ETR, and BLEND are very similar after 3–6 hr, although there exists obvious differences in the first 3 hr (Figures 13a and 13b) due to their different initial-error scale. This result indicates that the spatial scale of the initial perturbations (DOWN, ETR, and BLEND) has little impact on the later forecast (after 3–6 hr), suggesting an intrinsic predictability limit for this warm-sector torrential rainfall event to some extent.

5.2. Sensitivity to the Amplitude of Initial-Condition Uncertainties

Seven additional sensitivity forecasts, from GTOP1 to GTOP7, were conducted to investigate the sensitivity of the ensemble forecast to the magnitude of IC uncertainties. Similar to Melhauser and Zhang (2012) and Wu et al. (2013), these 24-hr sensitivity forecasts were initialized by linearly averaging the ICs of a GOOD member (ETR19) and a POOR member (BLEND11; Figures 14a and 14b). The GOOD member and POOR member are defined as GTOP0 and GTOP8, respectively. The ICs of each sensitivity forecast contained a fraction of the GTOP0 and GTOP8 ICs, with the weighting generated using equation (5):

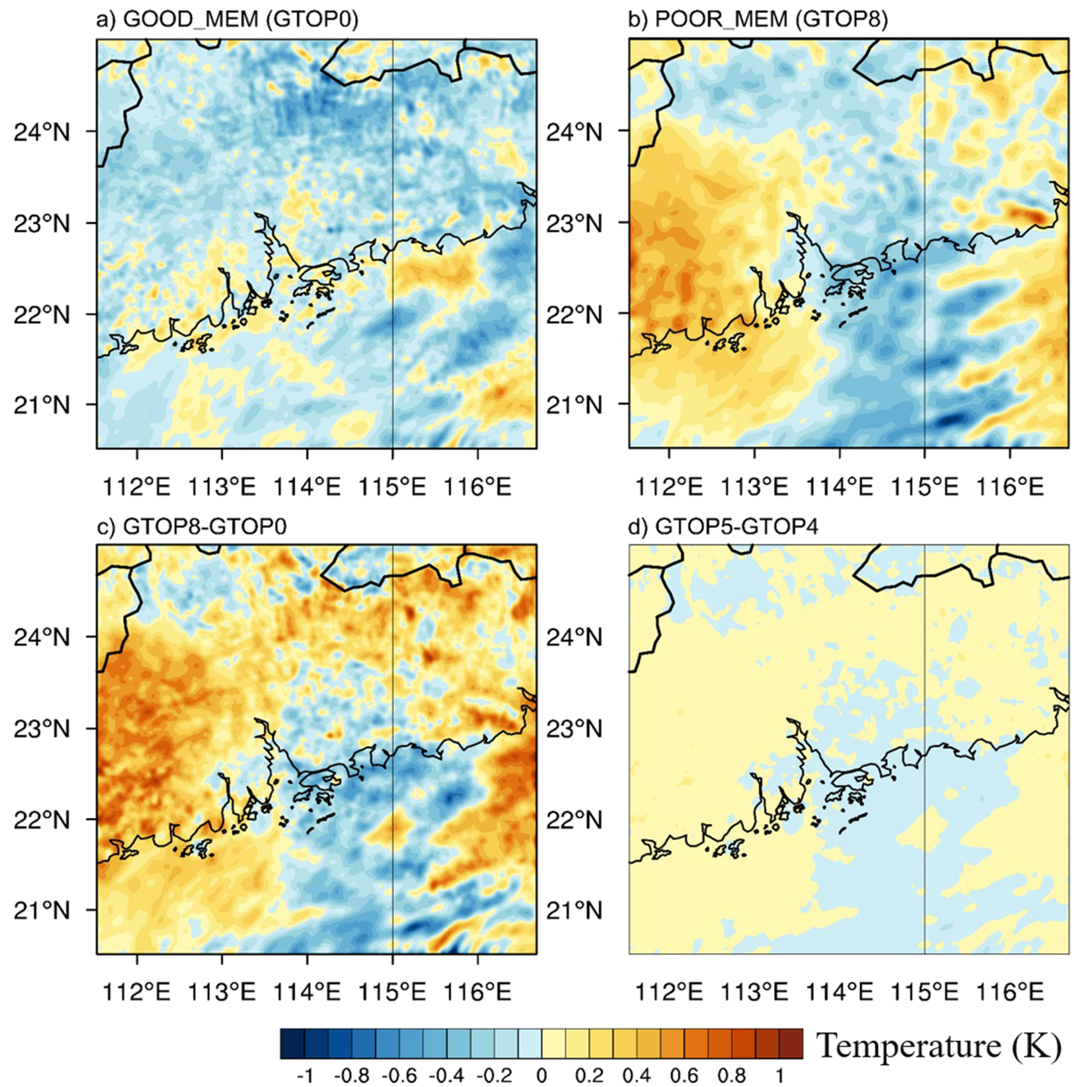

Figure 14. The distribution of initial temperature perturbations (shaded, °C; initialized at 0800 LST 19 May 2015) at 850 hPa for (a) a GOOD member (GTOP0), (b) a POOR member (GTOP8), (c) GTOP8 minus GTOP0, and (d) GTOP5 minus GTOP4.

$$\mathrm{GTOP}X = \frac{1}{8}[(8{-}X)\times\mathrm{GTOP0} + X\times\mathrm{GTOP8}], \tag{5}$$

where X is the sensitivity experiment number. As a fraction of the IC difference between GTOP0 and GTOP8, the difference between GTOP2 and GTOP6 is one half, between GTOP3 and GTOP5 is one quarter, and between GTOP4 and GTOP5 is one eighth, with the other members following the same division properties. In this GTOPX scaling process, all of the IC fields in domain D03 were perturbed, while the lateral boundary and the outer domain were not perturbed. As can be seen in Figures 14c and 14d, the difference in the distribution of 850-hPa initial temperature perturbation between GTOP5 and GTOP4 (less than 0.1 K) is much smaller than that between GTOP8 and GTOP0 (many areas exceed 0.5 K, with the maximum exceeds 1 K).

As in Zhang et al. (2003, 2006), the difference total energy (DTE), used to quantify the error growth procedure, was defined as

$$\mathrm{DTE} = \frac{1}{2}(u'u' + v'v' + kT'T'), \tag{6}$$

where u', v', and T' are the difference in wind components and difference in temperature between two simulations (two GTOPX), $k = C_p/T_r$ ($C_p = 1{,}004.9\ \mathrm{J \cdot kg^{-1} \cdot K^{-1}}$ and $T_r = 287$ K, the reference temperature). DTE

10.1029/2019JD031313

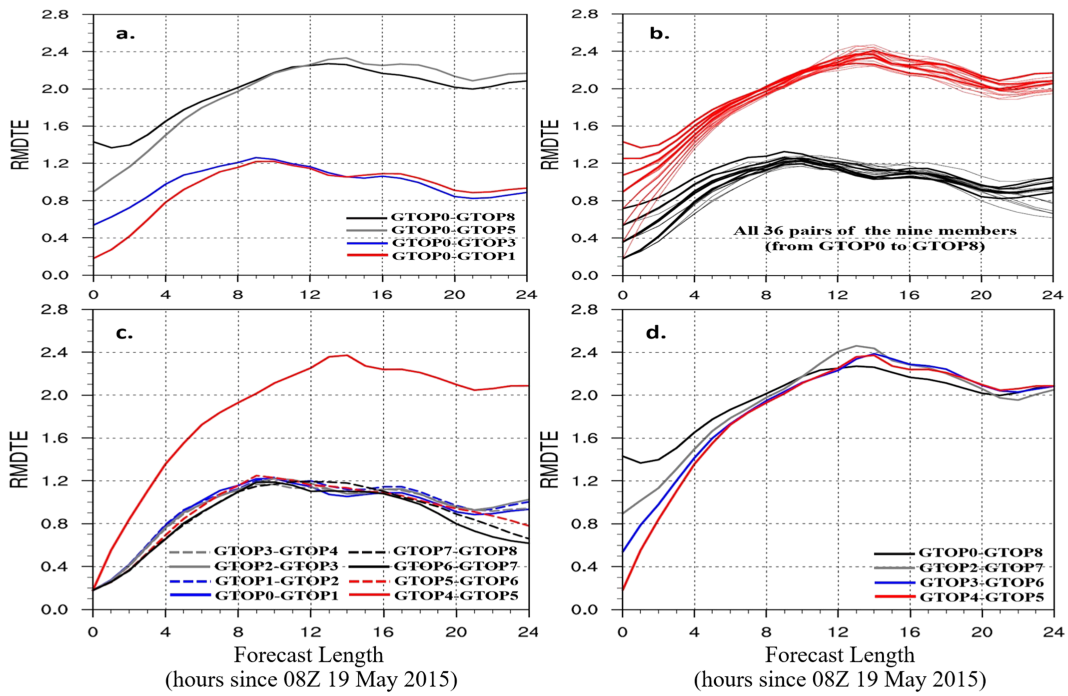

Figure 15. Temporal evolution of domain-averaged root-mean-difference total energy (RMDTE; m/s) between the indicated simulations from 0800 LST 19 May to 0800 LST 20 May 2015.

can be thought of as a representation of the energy difference from both thermodynamic and kinematic fields per unit mass between two simulations. A vertical function (pressure-weighted average) was further introduced to calculate the vertically integrated DTE, and the square root of the average DTE was defined to be the root-mean-difference total energy (RMDTE; Nielsen & Schumacher, 2016).

Figure 15a shows the temporal evolution of domain-averaged RMDTE for four pairs of the error-reducing sensitivity experiments (GTOP0−GTOP1, GTOP0−GTOP5, GTOP0−GTOP3, and GTOP0−GTOP1) from 0800 LST 19 May to 0800 LST 20 May. In terms of total RMDTE, the initial difference between GTOP0 and GTOP1 will be one eighth, nearly an order of magnitude less than GTOP0−GTOP8 at 0800 LST 19 May. It can be seen that a rapid increase in RMDTE appeared after the model initiation, in particular for the pairs with larger initial difference (GTOP0−GTOP8 and GTOP0−GTOP5). This feature of rapid error growth has been found in many previous studies, although there are some differences in the lead time and the rate of growth (Melhauser & Zhang, 2012; Nielsen & Schumacher, 2016; Zhang et al., 2006). Meanwhile, in contrast to the large-error pairs, the RMDTE of the small-error experiments (GTOP0−GTOP1 and GTOP0−GTOP3) show a slower increase, which seems to indicate that the event will have significant practical predictability.

However, from all of the 36 pairs of the nine members (GTOP0 to GTOP8), it can be seen that there were two sets of experiments with significant differences in the trend—one with rapid growth and large RMDTE (red lines), and the other with a more steady growth (black lines; Figure 15b). More importantly, although the RMDTEs of experiments with large errors (or large differences) are rapidly increasing, not all RMDTEs of experiments with small errors (or small differences) are slowly changing. From the eight pairs of experiments with the smallest differences, GTOP4−GTOP5 shows a rapid growth characteristic unlike the other seven pairs of experiments (Figure 15c). In fact, all the rapid-increase experiments (red lines in Figure 15b) include the difference of GTOP4−GTOP5, indicating that there might be a point of bifurcation between GTOP4 and GTOP5. From the simulated 3-hr accumulated rainfall for the nine forecasts (GTOP0 through GTOP8), we can also see clear divergence between the warm-sector convection development of GTOP4 and GTOP5 (Figure 16). The small differences in the ICs are manifesting themselves with (without) convective development in the coastal areas of GTOP4 (GTOP5), indicating that there is a dividing line or bifurcation point between the GTOP4 (developing) and the GTOP5 (non-developing) flow regimes.

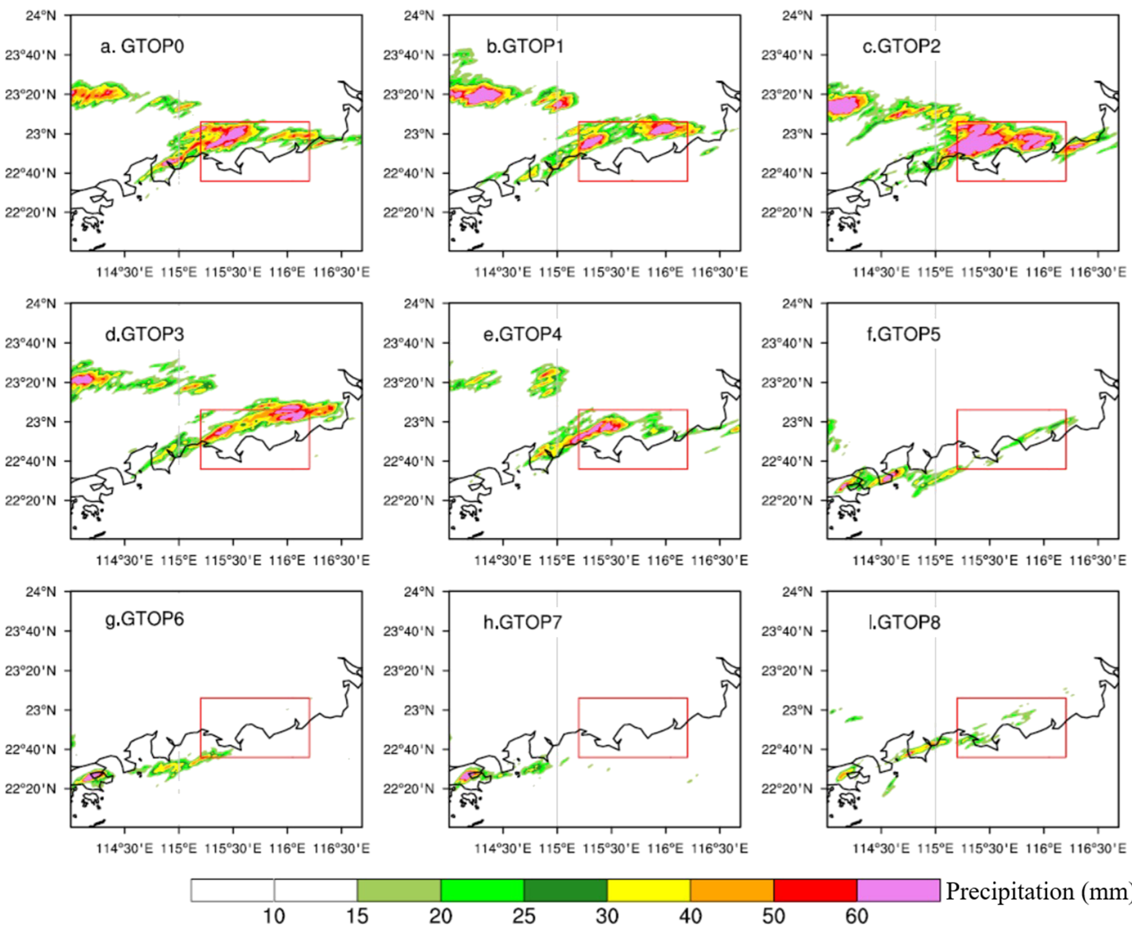

Figure 16. Simulated 3-hr accumulated rainfall (shaded, mm) for the linearly averaged sensitivity forecasts (GTOP0 through GTOP8) form 2200 LST 19 May to 0100 LST 20 May.

Figure 15d shows the four pairs of experiments with various differences, all of which include the difference of GTOP4−GTOP5. It can be seen that a rapid increase of RMDTE appeared after the model initiation in all of these four pairs. Meanwhile, by comparing the RMDTE of GTOP0 − GTOP8 to the subsequent three pairs of experiments with decreasing smaller initial differences, reducing the IC error does lead to a reduced final RMDTE and thus improves the practical predictability in the first 8 hr (0800 LST to 1600 LST 19 May), but at a decreasing rate. However, after 12 hr (2000 LST 19 May), the RMDTE of the three pairs with smaller initial differences are becoming larger than that of GTOP0 − GTOP8, indicating that an intrinsic predictability limit exists during this heavy rainfall event.

To further examine the variability of RMDTE according to the heavy rainfall, the evolution of domain-averaged RMDTE in the frontal rainfall region, warm-sector rainfall region, and the no-heavy-rain region are shown (Figure 17). In the frontal rainfall region (Region1), a rapid increase of RMDTE appears at 6 hr, and then the evolution of RMDTE in the four pairs of experiments is almost identical (Figure 17a). Besides, the pronounced diurnal cycle (i.e., an obvious reduction in RMDTE between 2000 LST 19 May and 0800 LST 20 May) present in Region1 indicates the (more predictable) synoptic front control on preventing the errors in this region from growing continuously, as in the MCS region (baroclinic zone) in Nielsen and Schumacher (2016).

In the warm-sector torrential rainfall region (Region2), however, a highly divergent feature of the temporal evolution of RMDTE exists between the four pairs of experiments (Figure 17b). In particular, by comparing the RMDTE of the four pairs of experiments with decreasing smaller initial differences, reducing the IC error does not lead to a reduced final RMDTE after 2000 LST 19 May. Conversely, the three pairs of experiments with the smaller difference, peaking at 15 hr, show a notably larger RMDTE than that of GTOP0−GTOP8

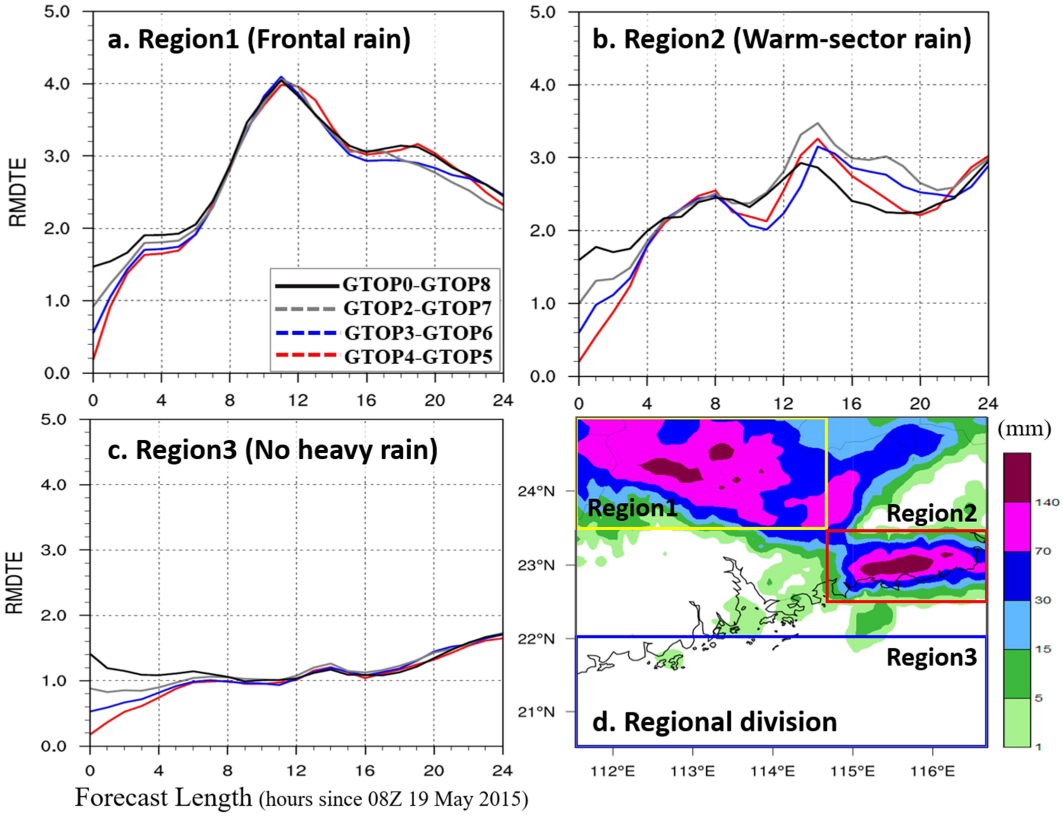

Figure 17. Temporal evolution of domain-averaged RMDTE (m/s) between the indicated simulations for the (a) region of frontal torrential rainfall (Region1), (b) region of warm-sector torrential rainfall (Region2), and (c) region of no heavy rainfall (Region3) from 0800 LST 19 May to 0800 LST 20 May 2015. (d) The regional division according to the precipitation (shaded, mm, as in Figure 2f).

during 2000 LST 19 May to 0400 LST 20 May (the major period of warm-sector torrential rainfall). This means that in the coastal warm-sector areas with deep moist convection, even if the initial error is reduced to one eight of the original, the subsequent forecast results are not necessarily better and may even be worse. On the other hand, the lack of a clear diurnal cycle (i.e., a reduction in RMDTE between 2000 LST 19 May and 0500 LST 20 May) and larger spread growth rates in Region 2 are associated with interactions with local terrain, land/mountain-breezes, and 925-hPa oceanic wind. It indicates that compared to the frontal rainfall region, this warm-sector heavy rainfall region has little change in the large-scale forcing through time, as in the MCV region of Nielsen and Schumacher (2016). In the no-heavy-rain region (Region3, a region with little to no convection), the RMDTEs are much smaller than in other regions (Figure 17c), probably due to the lack of deep moist convection (Nielsen & Schumacher, 2016). These sensitivity experiment results demonstrate that an intrinsic predictability limit exists for this coastal warm-sector torrential rainfall event.

As shown in the practical predictability analyses in section 4, nighttime strengthened southerly wind over the sea and nighttime cooling temperature over mountain areas are two key factors to the formation of warm-sector torrential rainfall. To depict the intrinsic predictability more specifically, we estimated the temporal evolutions of these two key factors in GTOP0, GTOP8, GTOP4, and GTOP5 (Figure 18). Compared to POOR member (GTOP8), the nighttime strengthened southerly wind (Figure 18a) and nighttime cooling temperature (Figure 18b) after 2000 LST 19 May could be better captured in the GOOD member (GTOP0). Although the initial differences of GTOP4−GTOP5 is only one eighth of GTOP0−GTOP8, similar differences exist for 925-hPa wind speed and near-surface temperature during the period of warm-sector torrential rainfall (2000 LST 19 May to 0800 LST 20 May). This indicates that under an environment of deep moist convection, the rapid growth of very small initial errors (GTOP4 and GTOP5) will also growth up rapidly and lead to significant differences in both nighttime southerly winds over the sea and near-surface temperature in

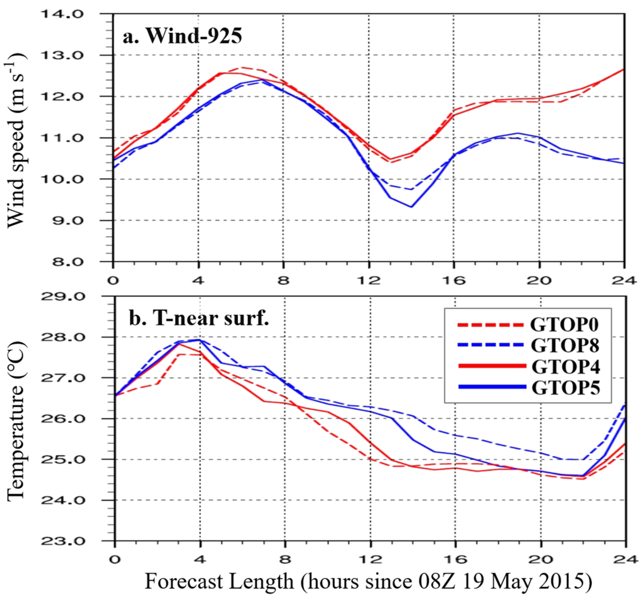

Figure 18. As in Figure 12 but for a specific GOOD member (GTOP0, red dotted line), POOR member (GTOP8, blue dotted line), and their corresponding experiments with tiny initial-condition difference (GTOP4 and GTOP5).

mountainous areas (Figure 18), which will result in an intrinsic predictability limit of coastal warm-sector torrential rainfall.

6. Summary and Discussion

The statistical characteristics and triggering mechanism of heavy rains in the South China monsoon region have been investigated from different aspects in previous studies, whereas how initial errors might grow at the mesoscale and how predictable they are is still not clear. In particular, the predictability of the frequent flash-flood-producing and low-forecasting-skill warm-sector torrential rainfall within weak synoptic forcing has not been documented. In this work, we examined the intrinsic and practical predictability of a warm-sector torrential rainfall event via convection-allowing ensemble forecasts (horizontal resolution of 1 km) during SCMREX on 19–20 May 2015.

Using a set of ICs that represented different spatial scales (Table 1) and small uncertainties (Table 2) with the WRF model, the 60 ensemble members showed large uncertainty with respect to the occurrence of coastal warm-sector torrential rainfall, indicating a chaotic divergence among them. Five convection-initiation and four nonconvection-initiation ensemble forecast members were subjectively chosen and their ICs averaged. By contrasting the PBL environments of the GOOD and POOR members, the CI of the warm-sector rainstorm was shown to be closely related to the low-level southerly wind over the sea, near-surface temperature over the northern mountain areas, and associated local meridional circulation.

Furthermore, investigation of the practical predictability of the coastal warm-sector torrential rainfall with the ESA method confirmed the results of the subset comparison (GOOD and POOR) and provided a more quantitative analysis of the low-level thermodynamic characteristics. A strengthening of the 925-hPa southerly flow over the northern South China Sea and a decrease in the near-surface temperature over the LHM would produce a higher maximum simulated precipitation in the warm-sector rainfall center 1–3 hr later. Improvements in the associated physical processes in NWP models for the nighttime strengthened southerly winds over the sea and cooling temperatures over the mountains are important to the practical predictability of warm-sector torrential rainfall. These analysis results of convection-allowing ensemble forecasts also verify the observational statistics reported in our pervious study (Wu et al., 2017).

For the intrinsic predictability, the sensitivity to the initial-error scale (synoptic scale, storm scale, and blending scale) and error growth at different scales were analyzed by introducing the decorrelation scale method. The spatial scale of the initial perturbations had little impact on the forecast after 3 hr and the meso-γ scales (2–20 km) of precipitation were fully decorrelated (complete loss of predictability) after 12 hr, highlighting an intrinsic predictability limit for this warm-sector torrential rainfall event.

Sensitivity experiments were conducted to linearly reduce the IC difference between a GOOD member and a POOR member by one half, one quarter, and one eighth, followed by integration for 24 h. The domain-averaged RMDTE indicated that improving the ICs by reducing the spread between ensemble members does not linearly decrease the final RMDTE. Conversely, after 8–12 hr, the RMDTE of the group with small-difference ICs appeared approaching and even exceeding the value of the group with large-difference ICs. This feature of nonlinear RMDTE development with IC differences is more obvious in the coastal warm-sector rainfall region than other regions, indicating a significant intrinsic predictability limit of warm-sector torrential rainfall. More specific results were also found in the temporal evolution of two important triggering factors (southerly winds over the sea and temperatures over the mountains) of the warm-sector rainfall in the tiny IC-difference experiments (GTOP4 and GTOP5).

In summary, from the perspective of practical predictability, improving the initial observations of the two sensitive thermodynamic factors (low-level winds over the sea and surface temperatures over the mountains) and the related model physics (e.g., the PBL scheme) can improve the forecasting ability of this coastal warm-sector torrential rainfall event. However, it should be noted that the practical predictability of severe weather is also influenced by some other factors in NWP models, such as horizontal resolution, physical parameterization schemes, and topographic effects (Surcel et al., 2015; Zhang et al., 2016; Burlingame et al., 2017). Recently, based on a 15-day period during the SCMREX in May 2014, Zhang (2018) specifically designed a convection-permitting ensemble prediction system to quantitative precipitation forecasts over southern China and found that initial perturbations, LBCs, and model physics were all very sensitive to different heavy rainfall events. Therefore, to improve the operational forecasting ability of warm-sector torrential rainfall, it is necessary to carry out more detailed studies with more operational practices and more flow-dependent cases (Melhauser & Zhang, 2012; Nielsen & Schumacher, 2016).

It should also be noted that different from the storm-scale predictability of some previous studies in which the environmental conditions are highly predictable (Zhang et al., 2015, 2016), there is a considerable intrinsic predictability limit of warm-sector torrential rainfall and its associated thermodynamic environmental conditions (Figures 12, 15, and 18). Therefore, a rapidly updating convection-allowing ensemble forecasting system should be a more effective tool for these warm-sector torrential rainfall events. However, the formulation of proper ensemble techniques at the meso or storm scale remains a highly challenging task (Johnson et al., 2014). Understanding more details about mesoscale predictability and corresponding error-growth dynamics could provide guidance on the design and implementation of convection-allowing ensemble forecast systems (Melhauser & Zhang, 2012; Zhang, 2018).

Acknowledgments
The authors express thanks to the Guangdong meteorological bureau of CMA for providing the observational data and UCAR for providing the NCEP-GFS analysis data (http://rda.ucar.edu/datasets/ds084.1/). This work was jointly supported by National Key R&D Program of China (2017YFC1502103), the National Natural Science Foundation of China (41705035), and the Science and Technology Planning Project of Guangdong Province, China (2017A020219005 and 2017B020244002). The simulations were performed on the High-Performance Computing Center of Nanjing University of Information Science and Technology. We also thank the anonymous reviewers for their helpful comments toward improving the original version of this paper.

References

Ancell, B. C., & Hakim, G. J. (2007). Comparing adjoint- and ensemble sensitivity analysis with applications to observation targeting. *Monthly Weather Review*, *135*, 4117–4134. https://doi.org/10.1175/2007MWR1904.1

Bauer, P., Thorpe, A., & Brunet, G. (2015). The quiet revolution of numerical weather prediction. *Nature*, *525*(7567), 47–55. https://doi.org/10.1038/nature14956

Bednarczyk, C. N., & Ancell, B. C. (2015). Ensemble sensitivity analysis applied to a southern plains convective event. *Monthly Weather Review*, *143*, 230–249. https://doi.org/10.1175/MWR-D-13-00321.1

Bei, N., & Zhang, F. (2007). Impacts of initial condition errors on mesoscale predictability of heavy precipitation along the Mei-Yu front of China. *Quarterly Journal of the Royal Meteorological Society*, *133*, 83–99.

Bierdel, L., Selz, T., & Craig, G. C. (2017). Theoretical aspects of upscale error growth through the mesoscales: An analytical model. *Quarterly Journal of the Royal Meteorological Society*, *143*, 3038–3059. https://doi.org/10.1002/qj.3160

Boustead, J. M., Mayes, B. E., Gargan, W.,Leighton, J. L., Phillips, G., & Schumacher, P. N. (2013). Discriminating Environmental Conditions for Significant Warm Sector and Boundary Tornadoes in Parts of the Great Plains. Wea. *Forecasting*, *28*, 1498–1523.

Browning, K. A., Hill, F. F., & Pardoe, C. W. (1974). Structure and mechanism of precipitation and the effect oforography ina wintertime warm sector. *Quarterly Journal of the Royal Meteorological Society*, *100*(425), 309–330.

Burlingame, B. M., Evans, C., & Roebber, P. J. (2017). The Influence of PBL parameterization on the practical predictability of convection initiation during the Mesoscale Predictability Experiment (MPEX). *Weather and Forecasting*, *32*, 1161–1183.

Caron, J. (2013). Mismatching Perturbations at the Lateral Boundaries in Limited-Area Ensemble Forecasting: A Case Study. *Monthly Weather Review*, *141*, 356–374. https://doi.org/10.1175/MWR-D-12-00051.1

Chen, X., Zhang, F., & Zhao, K. (2017). Influence of monsoonal wind speed and moisture content on intensity and diurnal variations of the Mei-yu season coastal rainfall over South China. *Journal of the Atmospheric Sciences*, *74*, 2835–2856.

Chen, X., Zhao, K., & Xue, M. (2014). Spatial and temporal characteristics of warm season convection over Pearl River Delta region, China, based on 3 years of operational radar data. *Journal of Geophysical Research: Atmospheres*, *119*, 12,447–12,465. https://doi.org/10.1002/2014JD021965

Cintineo, R. M., & Stensrud, D. J. (2013). On the predictability of Supercell thunderstorm evolution. *Journal of the Atmospheric Sciences*, *70*, 1993–2011.

Denis, B., Côté, J., & Laprise, R. (2002). Spectral decomposition of two-dimensional atmospheric fields on limited-area domains using discrete cosine transform (DCT). *Monthly Weather Review*, *130*, 1812–1829.

Ding, Y. (1994). Monsoons over China. *Advances in Atmospheric Sciences*, *11*, 252–252.

Done, J. M., Craig, G. C., Gray, S. L., & Clark, P. A. (2012). Case to case variability of predictability of deep convection in a mesoscale model. *Quarterly Journal of the Royal Meteorological Society*, *138*, 638–648. https://doi.org/10.1002/qj.943

Du, Y., & Chen, G. (2018). Heavy rainfall associated with double low-level jets over Southern China. Part I: Ensemble-based Analysis. *Monthly Weather Review*, *146*, 3827–3844.

Du, Y., & Chen, G. X. (2019). Heavy Rainfalls Associated with Double Low-level Jets over Southern China. *Part II: Convection initiation. Mon. Wea. Rev.*. *147*, 543–565.

Durran, D. R., & Gingrich, M. (2014). Atmospheric predictability: Why butterflies are not important. *Journal of the Atmospheric Sciences*, *71*, 2476–2488. https://doi.org/10.1175/JAS-D-14-0007.1

Durran, D. R., Reinecke, P. A., & Doyle, J. D. (2013). Large-scale errors and mesoscale predictability in Pacific Northwest snowstorms. *Journal of the Atmospheric Sciences*, *70*, 1470–1487. https://doi.org/10.1175/JAS-D-12-0202.1

Durran, D. R., & Weyn, J. A. (2016). Thunderstorms do not get butterflies. *Bulletin of the American Meteorological Society*, *97*, 237–243.

Hakim, G. J., & Torn, R. D. (2008). Ensemble synoptic analysis.Synoptic-Dynamic Meteorology and Weather Analysis andForecasting: A Tribute to Fred Sanders, *Meteor. Monogr.,No. 55, Amer. Meteor. Soc.*, 147–162. https://doi.org/10.1175/0065-9401-33.55.147

Hagedorn, R., Buizza, R., Hamill, T. M., Leutbecher, M., & Palmer, T. N. (2012). Comparing TIGGE multimodel forecasts with reforecast-calibrated ECMWF ensemble forecasts. *Quarterly Journal of the Royal Meteorological Society*, *138*, 1814–1827.

Hill, A. J., Weiss, C. C., & Ancell, B. C. (2016). Ensemble sensitivity analysis for mesoscale forecasts of dryline convection initiation. *Monthly Weather Review*, *144*, 4161–4182. https://doi.org/10.1175/MWR-D-15-0338.1

Hohenegger, C., Lüthi, D., & Schär, C. (2006). Predictability mysteries in cloud-resolving models. *Monthly Weather Review*, *134*, 2095–2107.

Hohenegger, C., & Schär, C. (2007a). Atmospheric predictability at synoptic versus cloud-resolving scales. *Bulletin of the American Meteorological Society*, *88*, 1783–1793.

Hohenegger, C., & Schär, C. (2007b). Predictability and error growth dynamics in cloud-resolving models. *Journal of the Atmospheric Sciences*, *64*, 4467–4478. https://doi.org/10.1175/2007JAS2143.1

Hong, S.,Dudhia, J., & Chen, S. (2004). A revised ap-proach to ice microphysical processes for the bulk parameterization of clouds and precipitation. *Monthly Weather Review*, *132*, 103–120.

Huang, S. S., Li, Z.-G., & Bao, C.-L. (1986). *Heavy rains in the first rainy season of South China (in Chinese)*, (p. 230). Guangzhou: Guangdong Science and Technology Press.

Iacono, M. J., Delamere, J. S., Mlawer, E. J., Shephard, M. W., Clough, S. A., & Collins, W. D. (2008). Radiative forcing by long-lived greenhouse gases: Calculations with the AER radiative transfer models. *Journal of Geophysical Research*, *113*, D13103. https://doi.org/10.1029/2008JD009944

Johnson, A., Kong, F., Zhao, G., Wang, Y., Thomas, K. W., Brewster, K. A., & Gao, J. (2014). Multiscale characteristics and evolution of perturbations for warm season convection allowing precipitation forecasts: Dependence on background flow and method of perturbation. *Monthly Weather Review*, *142*, 1053–1073. https://doi.org/10.1175/MWR-D-13-00204.1

Johnson, A., & Wang, X. (2016). A study of multiscale initial condition perturbation methods for convection-permitting ensemble forecasts. *Monthly Weather Review*, *144*, 2579–2604. https://doi.org/10.1175/MWR-D-16-0056.1

Liu, X., Luo, Y., Guan, Z., & Zhang, D. L. (2018). An extreme rainfall event in coastal South China during SCMREX-2014: Formation and roles of rainband and echo trainings. *Journal of Geophysical Research: Atmospheres*, *123*, 9256–9278. https://doi.org/10.1029/2018JD028418

Lorenz, E. N. (1963). Deterministic non-periodical flow. *Journal of the Atmospheric Sciences*, *20*, 130–141.

Lorenz, E. N. (1969). The predictability of a flow which possesses many scales of motion. *Tellus*, *21A*, 289–307.

Lorenz, E. N. (1982). Atmospheric predictability experiments with a large numerical model. *Tellus*, *34A*, 505–513.

Lorenz, E. N. (1996). *Predictability—A problem partly solved. Proc. Seminar on Predictability* (pp. 1–18). Reading, United Kingdom: ECMWF.

Luo, Y., Zhang, R., Wan, Q., Wang, B., Wong, W. K., Hu, Z., et al. (2017). The Southern China Monsoon Rainfall Experiment (SCMREX). *Bulletin of the American Meteorological Society*, *98*(5), 999–1013. https://doi.org/10.1175/BAMS-D-15-00235.1

Ma, J., Zhu, Y., Hou, D., Zhou, X., & Peña, M. (2014). Ensemble transform with 3D rescaling initialization method. *Monthly Weather Review*, *142*, 4053–4073. https://doi.org/10.1175/MWR-D-13-00367.1

Markowski, P., & Richardson, Y. (2010).Mesoscale meteorology in midlatitudes. Wiley-Blackwell, 132 pp.

Melhauser, C., & Zhang, F. (2012). Practical and intrinsic predictability of severe and convective weather at the mesoscales. *Journal of the Atmospheric Sciences*, *69*, 3350–3371. https://doi.org/10.1175/JAS-D-11-0315.1

Nielsen, E. R., & Schumacher, R. S. (2016). Using convection-allowing ensembles to understand the predictability of an extreme rainfall event. *Monthly Weather Review*, *144*, 3651–3676. https://doi.org/10.1175/MWR-D-16-0083.1

Oliver, V. J., & Shaw, R. F. (1956). Heavywarm-sector rains from illinois to middle atlantic coast, may 26–28, Mon. *Wea. Rev.*, *84*(5), 198–204.

Orlanski, I. (1975). A rational subdivision of scales for atmospheric processes. *Bulletin of the American Meteorological Society*, *56*, 527–530.

Palmer, T. N. (1993). Extended-range atmospheric prediction and the Lorenz model. *Bulletin of the American Meteorological Society*, *74*, 49–65.

Park, S. K. (1999). Nonlinearity and predictability of convective rainfall associated with water vapor perturbations in a numerically simulated storm. *Journal of Geophysical Research*, *104*, 31, 575–31, 587.

Rotunno, R., & Snyder, C. (2008). A generalization of Lorenz's model for the predictability of flows with many scales of motion. *Journal of the Atmospheric Sciences*, *65*, 1063–1076. https://doi.org/10.1175/2007JAS2449.1

Skamarock, W. C., Klemp, J. B., Dudhia, J., Gill, D. O., Barker, D., Duda, M. G., Huang, X.-Y., Wang, W., & Powers, J. G. (2008). A description of the Advanced Research WRF version 3. NCAR Tech. Note, NCAR/TN-4751STR, *NCAR/MMM*, 113. https://doi.org/10.5065/D68S4MVH

Stensrud, D. J., Bao, J. W., & Warner, T. T. (2000). Using initial condition and model physics perturbations in short-range ensemble simulations of mesoscale convective systems. *Monthly Weather Review*, *128*, 2077–2107.

Stensrud, D. J. (2007). *Parameterization Schemes: Keys to UnderstandingNumerical Weather Prediction Models*. CambridgeUniversity Press, 459 pp.

Sun, Y. Q., & Zhang, F. (2016). Intrinsic versus practical limits of atmospheric predictability and the significance of the Butterfly effect. *Journal of the Atmospheric Sciences*, *73*, 1419–1438.

Surcel, M., Zawadzki, I., & Yau, M. K. (2014). On the Filtering Properties of Ensemble Averaging for Storm-Scale Precipitation Forecasts. *Monthly Weather Review*, *142*, 1093–1105.

Surcel, M., Zawadzki, I., & Yau, M. K. (2015). A Study on the Scale Dependence of the Predictability of Precipitation Patterns. *Journal of the Atmospheric Sciences*, *72*, 216–235.

Tao, S., & Chen, L. (1987). A review of recent research on the East Asian summer monsoon in China. In C.-P. Chang & T. N. Krishnamurti (Eds.). *Monsoon Meteorology* (pp. 60–92). New York: Oxford University Press.

Thompson, P. D. (1957). Uncertainty of initial state as a factor in the predictability of large scale atmospheric flow patterns. *Tellus*, *9*, 275–295. https://doi.org/10.1111/j.2153-3490.1957.tb01885.x

Torn, R. D., & Hakim, G. J. (2008). Ensemble-based sensitivity analysis.*Monthly Weather Review*, *136*, 663–677. https://doi.org/10.1175/2007MWR2132.1

Torn, R. D., & Romine, G. S. (2015). Sensitivity of central Oklahoma convection forecasts to upstream potential vorticity anomalies during two strongly forced cases during MPEX. *Monthly Weather Review*, *143*, 4064–4087. https://doi.org/10.1175/MWR-D-15-0085.1

Toth, Z., & Kalnay, E. (1993). Ensemble forecasting at NMC: The generation of perturbation. *Bulletin of the American Meteorological Society*, *74*, 2317–2330. https://doi.org/10.1175/1520-0477(1993)074<2317:EFANTG>2.0.CO;2

Trapp, R. J., & Woznicki, J. M. (2017). Convectively induced stabilizations and subsequent recovery with supercell thunderstorms during the Mesoscale Predictability Experiment (MPEX). *Monthly Weather Review*, *145*, 1739–1754. https://doi.org/10.1175/MWR-D-16-0266.1

Walser, A., Lüthi, D., & Schär, C. (2004). Predictability of precipitation in a cloud-resolving model. *Monthly Weather Review*, *132*, 560–577.

Wandishin, M. S., Stensrud, D. J., Mullen, S. L., & Wicker, L. J. (2008). On the predictability of mesoscale convective systems: Two-dimensional simulations. *Weather and Forecasting*, *23*, 773–785.

Wandishin, M. S., Stensrud, D. J., Mullen, S. L., & Wicker, L. J. (2010). On the predictability of mesoscale convective systems: Three-dimensional simulations. *Monthly Weather Review*, *138*, 863–885.

Wang, H., Luo, Y.-L., & Jou, J.-D. (2014). Initiation, maintenance, and properties of convection in an extreme rainfall event during SCMREX: Observational analysis. *Journal of Geophysical Research: Atmospheres*, *119*, 13,206–13,232. https://doi.org/10.1002/2014JD022339

Wang, Y., Bellus, M., Geleyn, J.-F., Tian, W., & Weidle, F. (2014). A new method for generating initial condition perturbations in a regional ensemble prediction system: Blending. *Monthly Weather Review*, *142*, 2043–2059.

Wei, M., Toth, Z., Wobus, R., & Zhu, Y. (2008). Initial perturbations based on the ensemble transform (ET) technique in the NCEP global operational forecast system. *Tellus*, *60A*, 62–79. https://doi.org/10.1111/j.1600-0870.2007.00273.x

Weisman, M. L., Trapp, R. J., Romine, G. S., Davis, C., Torn, R., Baldwin, M., et al. (2015). The Mesoscale Predictability Experiment (MPEX). *Bulletin of the American Meteorological Society*, *96*, 2127–2149. https://doi.org/10.1175/BAMS-D-13-00281.1

Wu, D. C., Meng, Z. Y., & Yan, D. C. (2013). The predictability of a squall line in south China on 23 April 2007. *Advances in Atmospheric Sciences*, *30*, 485–502. https://doi.org/10.1007/s00376-012-2076-x

Wu, M., & Luo, Y. (2016). Mesoscale observational analysis of lifting mechanism of a warm-sector convective system producing the maximal daily precipitation in China mainland during pre-summer rainy season of 2015. *Journal of Meteorological Research*, *30*, 719–736.

Wu, N., Ding, X., Wen, Z., Chen, G., Meng, Z., Lin, L., & Min, J. (2020). Contrasting frontal and warm-sector heavy rainfalls over South China during the early-summer rainy season. *Atmospheric Research*, *235*, 10,4693. https://doi.org/10.1016/j.atmosres.2019.104693

Wu, N., Ding, X., Wen, Z., & Meng, Z. (2017). A comparison between warm-sector and frontal heavy rainfalls during the first rainy season in South China. Preprints, *17th Conference on Mesoscale Processes*, San Diego, CA, Amer. Meteor. Soc., 16.2.

Xia, R.-D., Zhao, S.-X., & Sun, J.-H. (2006). Analysis and study on environment characteristics of the Class-1 β mesoscale system in the warm sector ahead of front in South China (in Chinese). *Atmospheric Sciences*, *30*, 988–1007.

Xu, W., Zipser, E. J., Chen, Y., Liu, C., Liou, Y., Lee, W., & Jou, B. J.-D. (2012). An orography-associated extreme rainfall event during TiMREX: Initiation, storm evolution, and maintenance. *Monthly Weather Review*, *140*(8), 2555–2574. https://doi.org/10.1175/MWR-D-11-00208.1

Yu, H., & Meng, Z. (2016). Key synoptic-scale features influencing the high-impact heavy rainfall in Beijing, China on 21 July 2012. *Tellus A*, *68*, 31,045.

Zhang, F., Bei, N., Rotunno, R., Snyder, C., & Epifanio, C.-C. (2007). Mesoscale predictability of moist baroclinic waves: Convection-permitting experiments and multistage error growth dynamics. *Journal of the Atmospheric Sciences*, *64*, 3579–3594.

Zhang, F., Odins, A. M., & Nielsen-Gammon, J. W. (2006). Mesoscale predictability of an extreme warm-season precipitation event. *Weather and Forecasting*, *21*, 149–166.

Zhang, F., Snyder, C., & Rotunno, R. (2003). Effects of moist convection on mesoscale predictability. *Journal of the Atmospheric Sciences*, *60*, 1173–1185.

Zhang, M., & Meng, Z. (2018). Impact of synoptic-scale factors on rainfall forecast in different stages of a persistent heavy rainfall event in South China. *Journal of Geophysical Research – Atmospheres*, *123*, 3574–3593. https://doi.org/10.1002/2017JD028155

Zhang, X. (2018). Application of a convection-permitting ensemble prediction system to quantitative precipitation forecasts over southern China: Preliminary results during SCMREX. *Quarterly Journal of the Royal Meteorological Society*, *144*, 2842–2862.

Zhang, X.-M., Meng, W.-G., Zhang, Y.-X., & Liang, J.-Y. (2011). Analysis of mesoscale convective systems associated with a warm-sector heavy rains event over South China. *Journal of Tropical Meteorology*, *17*, 1–10.

Zhang, C., & Wang, Y. (2017). Projected Future Changes of Tropical Cyclone Activity over the Western North and South Pacific in a 20-Km-Mesh Regional Climate Model. *Journal of Climate*, *30*(15), 5923–5941.

Zhang, Y., Zhang, F., Stensrud, D.-J., & Meng, Z.-Y. (2015). Practical predictability of the 20 May 2013 tornadic thunderstorm event in Oklahoma: Sensitivity to synoptic timing and topographical influence. *Monthly Weather Review*, *143*, 2973–2997. https://doi.org/10.1175/MWR-D-14-00394.1

Zhang, Y., Zhang, F., Stensrud, D.-J., & Meng, Z.-Y. (2016). Intrinsic predictability of the 20 May 2013 tornadic thunderstorm event in Oklahoma at storm scales. *Monthly Weather Review*, *144*, 1273–1298. https://doi.org/10.1175/MWR-D-15-0105.1